Atmospheric inversion of SO2 and primary aerosol emissions for the year 2010

N. Huneeus, O. Boucher, F. Chevallier

Atmos. Chem. Phys., 13, 6555–6573, 2013
www.atmos-chem-phys.net/13/6555/2013/
doi:10.5194/acp-13-6555-2013

Atmospheric Chemistry and Physics Open Access

Atmospheric inversion of SO_2 and primary aerosol emissions for the year 2010

N. Huneeus[1], O. Boucher[1], and F. Chevallier[2]

[1]Laboratoire de Météorologie Dynamique, IPSL, UMR8539, CNRS/UPMC, Paris, France
[2]Laboratoire des Sciences du Climat et de l'Environnement, IPSL, UMR8212, CEA-CNRS-UVSQ, Gif-sur-Yvette, France

Correspondence to: N. Huneeus (nicolas.huneeus@lmd.jussieu.fr)

Received: 7 January 2013 – Published in Atmos. Chem. Phys. Discuss.: 7 March 2013
Revised: 6 June 2013 – Accepted: 9 June 2013 – Published: 11 July 2013

Abstract. Natural and anthropogenic emissions of primary aerosols and sulphur dioxide (SO_2) are estimated for the year 2010 by assimilating daily total and fine mode aerosol optical depth (AOD) at 550 nm from the Moderate Resolution Imaging Spectroradiometer (MODIS) satellite instrument into a global aerosol model of intermediate complexity. The system adjusts monthly emission fluxes over a set of predefined regions tiling the globe. The resulting aerosol emissions improve the model performance, as measured from usual skill scores, both against the assimilated observations and a set of independent ground-based measurements. The estimated emission fluxes are 67 Tg S yr^{-1} for SO_2, 12 Tg yr^{-1} for black carbon (BC), 87 Tg yr^{-1} for particulate organic matter (POM), 17 000 Tg yr^{-1} for sea salt (SS, estimated at 80 % relative humidity) and 1206 Tg yr^{-1} for desert dust (DD). They represent a difference of +53, +73, +72, +1 and −8 %, respectively, with respect to the first guess (FG) values. Constant errors throughout the regions and the year were assigned to the a priori emissions. The analysis errors are reduced with respect to the a priori ones for all species and throughout the year, they vary between 3 and 18 % for SO_2, 1 and 130 % for biomass burning, 21 and 90 % for fossil fuel, 1 and 200 % for DD and 1 and 5 % for SS. The maximum errors on the global-yearly scale for the estimated fluxes (considering temporal error dependence) are 3 % for SO_2, 14 % for BC, 11 % for POM, 14 % for DD and 2 % for SS. These values represent a decrease as compared to the global-yearly errors from the FG of 7 % for SO_2, 40 % for BC, 55 % for POM, 81 % for DD and 300 % for SS. The largest error reduction, both monthly and yearly, is observed for SS and the smallest one for SO_2. The sensitivity and robustness of the inversion system to the choice of the first guess emission inventory is investigated by using different combinations of inventories for industrial, fossil fuel and biomass burning sources. The initial difference in the emissions between the various set-ups is reduced after the inversion. Furthermore, at the global scale, the inversion is sensitive to the choice of the BB (biomass burning) inventory and not so much to the industrial and fossil fuel inventory. At the regional scale, however, the choice of the industrial and fossil fuel inventory can make a difference. The estimated baseline emission fluxes for SO_2, BC and POM are within the estimated uncertainties of the four experiments. The resulting emissions were compared against projected emissions for the year 2010 for SO_2, BC and POM. The new estimate presents larger emissions than the projections for all three species, with larger differences for SO_2 than POM and BC. These projected SO_2 emissions are outside the uncertainties of the estimated emission inventories.

1 Introduction

Aerosols play an important role in air quality, atmospheric visibility and climate. Concentration levels of particulate matter below 2.5 and 10 µm at the surface are used as indicators of air quality and are known to have an adverse impact on human health (Keuken et al., 2011; Pérez et al., 2010). Aerosols also affect climate through their impact on the Earth's energy balance either through their interactions with atmospheric radiation (absorption and scattering of solar radiation; absorption, scattering and emission of terrestrial radiation) or their interactions with clouds. Both types of interactions are known to perturb the hydrological cycle

through changes in the atmospheric and surface energy budget, induced changes in atmospheric circulation, and changes to the cloud microphysical evolution, but the respective importance of these effects is poorly understood (Haywood and Boucher, 2000; Forster et al., 2007; Denman et al., 2007). Finally, aerosols play a significant role in tropospheric chemistry through heterogeneous chemistry on their surface (Bauer et al., 2004; Zhu et al., 2010).

Currently aerosols represent the largest source of uncertainty when estimating the total anthropogenic radiative forcing (Haywood and Schulz, 2007). A significant part of this uncertainty is due to a lack of knowledge on the spatial and temporal distribution of aerosol emissions (Lee et al., 2011). Such knowledge is needed to quantify the impact of aerosols on climate and air quality in regional and global aerosol models.

Natural emissions of desert dust (DD) and sea-salt (SS) aerosols are either prescribed in such models or interactively calculated as a function of surface wind speed and other local surface and atmospheric variables. Actual measurements characterizing dust and sea-salt emission processes, either in controlled environments (such as in a wind tunnel) or in the real world, remain limited (e.g., O'Dowd et al., 1997; Alfaro et al., 2004; Rajot et al., 2003; Roney and White, 2006; Sweeney et al., 2008; Sow et al., 2009). Parameterizations of emissions either are empirical, as it is often the case for sea-salt aerosols (de Leeuw et al., 2011), or combine a physical basis with a more empirical diagnostic of source areas, as is sometimes done for dust (Marticorena et al., 2004). For instance, Ginoux et al. (2012) compute global dust emissions by combining source hot spots based on Moderate Resolution Imaging Spectroradiometer (MODIS) Deep Blue estimates of dust optical depth with other information on land use and presence of ephemeral water bodies. Model emissions are often validated indirectly through an assessment of the model performance in simulating atmospheric concentrations, surface deposition fluxes and/or aerosol optical depth (Ginoux et al., 2001; Tegen et al., 2002; Laurent et al., 2008; Huneeus et al., 2011). The different ways to parameterize these emissions, the choice of input data to these parameterizations and the differences in the simulated particle size (e.g. maximum size distribution for DD can vary between 8.0 to 25 µm) explain the large diversity in the dust and sea-salt emissions (Textor et al., 2006; Huneeus et al., 2011).

The emissions of anthropogenic primary aerosols and sulphur dioxide (SO_2) from fossil-fuel combustion and industrial activity are estimated from so-called "bottom-up" approaches. These methods combine information such as energy consumption, combustion efficiency, emission factors and mitigation technology to compute disaggregated emissions fluxes. Numerous studies have been conducted in this way to estimate the emission on both the regional (e.g. Qin and Xie, 2012; Lu et al., 2010, 2011) and global scale (e.g. Olivier et al., 2005; Bond et al., 2004; van Aardenne et al., 2001). Such studies have focused on specific sectors (Eyring et al., 2010; Wang et al., 2011; Assamoi and Liousse, 2010) or estimated the emissions from all sectors relying on fossil fuels (e.g. Junker and Liousse, 2008). They have been centred on a given species (e.g. Smith et al., 2011) or estimated simultaneously the emissions of a range of species (e.g. Dentener et al., 2006; Zhang et al., 2009; Lamarque et al., 2010; Diehl et al., 2012). Some of these inventories not only considered present-day emissions but also past emissions over some period (e.g. Lei et al., 2011; Streets et al., 2008; Ohara et al., 2007). A thorough intercomparison of several of these inventories is provided in Granier et al. (2011).

Building an inventory of anthropogenic emissions relies on various sources of information available from governments, international organizations, research centres and in the literature, in particular for emission factors (e.g. Junker and Liousse, 2008; Olivier et al., 2005; Wang et al., 2011). The uncertainties associated with these inventories are difficult to estimate and there have been only a few attempts to quantify them (e.g. Bond et al., 2004; Smith et al., 2011). They depend on the quality and uncertainties of the underlying information, but also on the methods used to deal with missing information. In addition, studies estimating primary aerosol emissions are very time demanding and are not conducted on a regular basis. As a result a considerable time lag, as long as 5 to 10 yr, often exists between a given target period and the moment the inventory is produced.

Biomass burning emissions of SO_2 and primary aerosols, black carbon (BC) and organic carbon (OC) among others, are usually estimated as the product of burned area, areal fuel loads, combustion completeness and emission factors. A commonly used inventory is the Global Fire Emissions Database (GFED, van der Werf et al., 2006, 2010) that uses burned areas product from MODIS. A similar approach was used by Hoelzemann et al. (2004) to estimate the wildland fire emissions for the year 2000 using burned area from the Global Burnt Scar satellite product (GLOBSCAR). More recently, the Global Fire Assimilation System (GFAS), developed by Kaiser et al. (2012), computes biomass burning emissions by combining fire radiative power (FRP) from the MODIS instrument with land surface characteristics. Other estimates of biomass burning emissions exist that combine bottom-up inventories with some satellite data (Streets et al., 2003; Generoso et al., 2003; Ito and Penner, 2005; Vermote et al., 2009).

In the last decade top-down (or inversion) techniques have been developed that estimate aerosol emission by combining satellite data and numerical models. An important technique for this purpose is data assimilation, where observational data is combined with numerical models to find a statistically optimal solution that represents the best compromise between a priori (or first guess) information and observations. Zhang et al. (2005) estimated biomass burning emissions for 1997 by assimilating the Total Ozone Mapping Spectrometer (TOMS) aerosol index. Hakami et al. (2005) used a variational data assimilation approach to estimate BC

emissions and initial conditions over East Asia by assimilating concentration measurements. Yumimoto et al. (2007, 2008) applied the same approach to estimate dust emissions for dust events by assimilating lidar observations. Dubovik et al. (2008) estimated the emissions of fine and coarse mode aerosols for a period of two weeks in August 2000 by assimilating MODIS aerosol optical depth (AOD) at 550 nm in the Goddard Chemistry Aerosol Radiation and Transport (GOCART) aerosol model. Fu et al. (2012) estimated the emissions of carbonaceous aerosols in China constraining the fluxes with surface concentration measurements. Finally, Huneeus et al. (2012) presented the first study to estimate simultaneously the global emissions for multiple aerosol species and one gaseous precursor, namely DD, SS, BC, particulate organic matter (POM) and SO_2. The authors estimated the emissions in a consistent and coherent manner by assimilating daily total and fine mode AOD at 550 nm from MODIS into an aerosol model of intermediate complexity.

This study builds on the work presented in Huneeus et al. (2012), hereafter denoted HCB12, where a detailed description of the assimilation system as well as an assessment of its preliminary application to estimate the aerosol and SO_2 emissions for the year 2002 were given. In the present study we have improved our treatment of uncertainties and have updated the a priori emissions inventory and the choice of target regions for the source inversion. We produce here a monthly and regional calibration of emissions of anthropogenic primary aerosols and SO_2 as well as monthly emissions of natural aerosols of DD and SS at the model resolution for the year 2010. We also explore the sensitivity of the results to the choice of the a priori emission inventories from fossil fuel and biomass burning sources. No sensitivity analysis is conducted on natural emissions of DD and SS given the absence of a reference emission inventory on one hand and the physical nature of their emissions on the other hand. Section 2 presents a brief description of the different components of the inversion system, focusing on the evolution since the HCB12 study. In Sect. 3 we describe the different emission inventories used as a priori and present in Sect. 4 the estimated emissions for each inventory. We present the main conclusions of this work in Sect. 5.

2 Assimilation system

The monthly emissions of BC, POM, DD, SS and SO_2 are estimated by assimilating fine mode and total aerosol optical depth into a model of intermediate complexity. The method applied is the same as used in HCB12, however, improvements have been introduced in the definition of the emission regions (Sect. 2.3), the assignment of the emission error statistics (Sect. 2.4), and the emissions used as a priori (Sect. 3). A brief description of the system and the introduced changes will be given in the present section but the reader should refer to HCB12 for more details about the assimilation system.

2.1 Assimilation method

The estimated emission fluxes in this study represent the best compromise between the observations $\boldsymbol{y}$ and the a priori information $\boldsymbol{x}^b$. This optimal state vector $\boldsymbol{x}^a$, also known as analysis, is found by minimizing a cost function J. This cost function is defined as the sum of the departures of a potential solution $\boldsymbol{x}$ and of the corresponding simulated observations to the a priori information $\boldsymbol{x}^b$ and to the given observations $\boldsymbol{y}$:

$$J(\boldsymbol{x}) = 1/2(\boldsymbol{x}-\boldsymbol{x}^b)^{\mathrm{T}}\mathbf{B}^{-1}(\boldsymbol{x}-\boldsymbol{x}^b) + 1/2(H(\boldsymbol{x})-\boldsymbol{y})^{\mathrm{T}}\mathbf{R}^{-1}(H(\boldsymbol{x})-\boldsymbol{y}), \quad (1)$$

where H is the non-linear observation operator that computes the equivalent of the observations $\boldsymbol{y}$ for a given state vector $\boldsymbol{x}$, $\mathbf{R}$ is the covariance matrix of the error statistics of the observations and $\mathbf{B}$ is the covariance matrix of the error statistics of the a priori information (Rodgers, 2000). The superscript T denotes the transpose.

The method used to minimize the cost function J depends among other aspects on the size of the state vector as well as the relative sizes of the $\mathbf{B}$ and $\mathbf{R}$ matrixes and the difficulties associated with their inversion (Chevallier et al., 2005). Considering the relatively small size of our state vector (Sect. 2.3) and the fact that $\mathbf{R}$ is defined as a diagonal matrix (Sect. 2.4) and is thus easy to invert, we compute the analysis through the following analytical formulation:

$$\boldsymbol{x}^a = \boldsymbol{x}^b - (\mathbf{H}^{\mathrm{T}}\mathbf{R}^{-1}\mathbf{H} + \mathbf{B}^{-1})^{-1}\mathbf{H}^{\mathrm{T}}\mathbf{R}^{-1}(\mathbf{H}\boldsymbol{x}^b - \boldsymbol{y}), \quad (2)$$

where $\mathbf{H}$ is the linearized operator of H.

As observation operator, we use the simplified aerosol model (hereafter SPLA) which has been documented in Huneeus et al. (2009). This model computes the fine mode and total AOD at three wavelengths, 550, 670 and 865 nm. It was derived from the aerosol model embedded in the general circulation model of the Laboratoire de Météorologie Dynamique (LMDZ) (Reddy et al., 2005). The SPLA model groups the 24 original tracers simulated in LMDZ into four tracers, namely the gaseous precursors, the fine mode aerosols, the coarse sea salt aerosols and the coarse desert dust aerosols. The gaseous aerosol precursor groups dimethyl sulphide (DMS), SO_2 and hydrogen sulphide (H_2S) together. The aerosol fine mode includes sulphate (SU), BC, POM, DD with radii between 0.03 and 0.5 µm and SS aerosols with radii smaller than 0.5 µm. The SS coarse mode groups together particles with radii between 0.5 and 20 µm whereas the coarse DD mode corresponds to particles with radii between 0.5 and 10 µm. It should be noted that emissions for each aerosol species and gaseous precursor are estimated as in the original model; in particular the SS flux is estimated for aerosols at 80 % relative humidity. These emissions are

then lumped together to serve as emissions for our four tracers, which are then treated as such in the model. New values of deposition velocities, mass median diameter and mass extinction efficiencies were recomputed according to the definition of the new tracers. Furthermore, the sulphur chemistry was reduced to an oxidation mechanism as a function of latitude and no distinction between hydrophilic and hydrophobic OM and BC was made. The timescale for SO_2 oxidation varies as the cosine of the latitude from 1 day at the Equator to 5 days at the poles (instead of 3 and 8 days, respectively, in the original HCB12 study).

2.2 Observations

The daily total AOD over land and ocean and the fine mode AOD over ocean only are assimilated. Both of these AOD products are at 550 nm. The data is extracted from the ICARE Data and Services Centre (http://www.icare.univ-lille1.fr) where the aerosol products from multiple sensors are generated and/or archived.

Data from the MODIS instrument onboard the Terra satellite are used, specifically, the daily level 3 aerosol products (MOD08) from collection 5.1. These level 3 data are averaged on a $1^\circ \times 1^\circ$ grid (MOD08_D3). Only the daily product is included in our assimilation procedure and thus the time of the measurement within the day is not considered. We apply an additional quality check besides those already included in the production of level 3 AOD MODIS product. In the original processing, the level 3 AOD data are weighted by the quality of each individual retrieval in order to prevent poor retrievals from affecting the calculated statistics (Remer et al., 2005; King et al., 2003; Hubanks et al., 2008). By applying an additional quality check over ocean and over land we seek to remove outliers and biases. We base our data screening on the method described in Zhang and Reid (2006) which we apply to both the total and fine mode AOD. We remove retrievals with an AOD larger than 3 over ocean and only consider $1^\circ \times 1^\circ$ grid boxes with cloud fraction less than 80 %. In contrast to Zhang et al. (2008) we apply the cloud fraction threshold also over land. In addition, we remove all pixels south of 40° S to ensure that the known overestimation of AOD over the Southern Hemisphere oceans southward from 40° S does not impact the assimilation system negatively (Zhang and Reid, 2006). Finally, the MODIS data are thinned from their original resolution ($1^\circ \times 1^\circ$) to the coarser model resolution ($3.75^\circ \times 2.5^\circ$).

2.3 State vector

We assume, based on the dominant uncertainty about the emission factors (EF) in the emission error budget, that prior emission errors are dominated by time-independent (over two-month periods) and spatially homogeneous patterns, within large regions and for each emission type. This assumption allows us to define a relatively short state vector, and therefore, to reduce the computational cost of the inversion. To implement the above and further limit the computational cost, the number of tracers was reduced from 24 in the original model to 4 in SPLA (Sect. 2.1). In addition, an assimilation window of two months was defined allowing the inversion to be independent from the initial aerosol concentrations. The results from an inversion cycle are considered to be representative of the last month. Finally, the emission regions were defined so that the main emission processes were isolated from each other and sources with opposite seasonality do not belong to the same region. The result of our data assimilation system is to uniformly increase or decrease the emissions of each aerosol species within each region.

For fine and coarse SS, a single global region was defined as this source term stems from a physical mechanism that should be the same everywhere. For SO_2, the eight regions originally defined in HCB12 have been increased to 13 (Fig. 1a) to better represent different levels of development (and therefore emissions) between the regions. The original region of North America has been split into Central and North America in order to separate Mexico from the USA and Canada. Region Northern Africa in HCB12 has been divided into Northern and Central Africa to account for possible underestimations in emissions in central African countries as suggested by Assamoi and Liousse (2010). Countries of the Middle East that were located in the African and Asian regions in HCB12 are now grouped together in one region. In addition, the Asian region has been separated into Russia and East Asia. The latter groups together the countries of China, Mongolia, South and North Korea and Japan. Finally, South Asia was split into India and South East Asia. The former includes India, Pakistan, Bhutan, Nepal, Bangladesh and Sri Lanka. The BC and POM emission regions were defined differently for biomass burning (BB) or fossil fuel (FF) combustion sources. The definition of the biomass burning regions is based on the 14 regions defined in the GFED (van der Werf et al., 2006) inventory. However, a few modifications have been introduced to this regional definition. The Southern Hemisphere South America (SHSA) region defined in GFED has been divided into two regions, namely Central South America (CESA) and Southern South America (SSAM) to account for the differences in vegetation type between these two regions (G. R. van der Werf, personal communication, 2013). In addition, the Middle East (MIDE) and Northern Hemisphere Africa (NHAF) regions defined in GFED have been combined into a single region, namely North Africa and Middle East (NAME), because of the limited biomass burning emissions in MIDE (G. R. van der Werf, personal communication, 2013). Finally, the GFED Central Asia (CEAS) region has been split into Inner Asia (INAS) and China to facilitate the comparison with existing biomass burning inventories for China. The 15 biomass burning regions are illustrated in Fig. 1b. For FF emissions the same 13 regions defined for SO_2 are used (Fig. 1a). These regions will be referred to as industrial (IND) hereafter. Finally, we use the

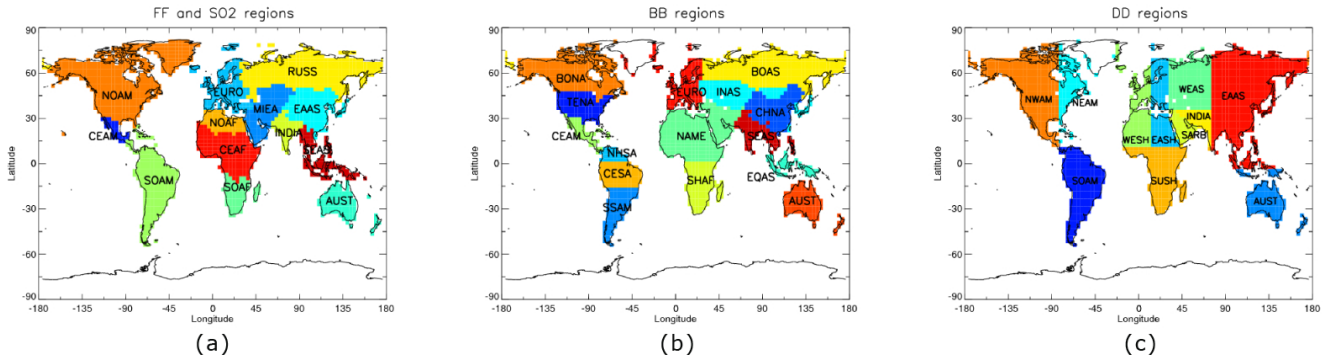

Fig. 1. Definition of emission regions used in the control vector for SO_2 and the different aerosol species. **(a)** Thirteen regions are defined for emissions of both SO_2 and other FF aerosols: North, Central and South America (NOAM, CEAM, and SOAM, respectively), Europe (EURO), North, Central and South Africa (NOAF, CEAF, and SOAF, respectively), Middle East (MIEA), Russia (RUSS), India (INDIA), East Asia (EEAS), South East Asia (SEAS) and Australia (AUST). **(b)** Fifteen regions are defined for BB aerosol emissions: Boreal North America (BONA), Temperate North America (TENA), Central America (CEAM), Northern Hemisphere South America (NHSA), Central South America (CESA), Southern South America (SSAM), Europe (EURO), North Africa and Middle East (NAME), Southern Hemisphere Africa (SHAF), Inner Asia (INAS), Boreal Asia (BOAS), China (CHNA), South East Asia (SEAS) Equatorial Asia (EQAS) and Australia (AUST). Biomass burning regions are based on GFED regions (Sect. 2.3). **(c)** Eleven regions are defined for dust emissions: North West America (NWAM), North East America (NEAM), South America (SOAM), Western Sahara (WESH), Eastern Sahara (EASH), Sub-Sahara (SUSH), Western Asia (WEAS), India (INDIA), Saudi Arabia (SARB), East Asia (EAAS) and Australia (AUST).

same eleven dust regions separating the main global deserts as defined in HCB12 to estimate dust emission for each one of the fine and coarse modes (Fig. 1c).

In summary, the state vector consists of 65 elements with two global parameters for fine and coarse SS, 22 regional parameters for fine and coarse DD, 13 for SO_2, 13 for FF and finally, 15 for BB regions.

The anthropogenic emissions used as first guess for FF and SO_2 (Sect. 3) consider emissions from ten active sectors, namely energy production and distribution, industry, land transport, maritime transport, residential and commercial, solvents, agriculture, agriculture waste burning on fields and waste. Only emissions associated to energy, industry, land transport and residential and commercial emissions are considered active and are therefore estimated. These emissions are increased/decreased by the inversion in each region in the same proportion for each active sector. Emissions from agricultural waste burning emissions are not included in the study since they are considered to be included in the biomass burning inventory. The remaining emission fluxes included in the model (i.e. dimethyl sulphide, volcanic SO_2, emissions from shipping and biogenic secondary organic aerosols) are not considered in the state vector and are therefore not optimized. The contribution of a number of small volcanoes to stratospheric AOD (not represented in the model) remains fairly small (~ 0.003) for the period of interest in this study and is therefore unlikely to affect significantly our inversion and the conclusions which are drawn (Vernier et al., 2011).

2.4 Error covariances

The matrices **B** and **R** (Eq. 1) describe the error statistics of the emission fluxes and of the observations, respectively. Their relative magnitude determines the weight given to the a priori information and to the observations. The error values presented in this section and hereafter correspond to one standard deviation except when stated otherwise.

We follow HCB12 and define **B** as a diagonal matrix neglecting the possible prior error correlations between two species within one region and for a given species between regions. However, in view of the new definition of the state vector (Sect. 2.3) and the use of more updated a priori emission inventories (Sect. 3) we have redefined the monthly emission uncertainties for this work. We consider monthly regional emission uncertainties of 130 % for BB and 90 % for combustion of FF. These values are based on the emission range for BC and OC of open biomass burning and of contained combustion given in Bond et al. (2004). For SO_2 emissions we define the uncertainty in monthly regional emission to be 18 % in accordance to the estimate in Smith et al. (2011). The authors in this work estimated that the regional uncertainty could range up to 30 %. To our knowledge, no documented estimate of uncertainties in the natural emissions of DD and SS exist and we therefore use the diversity of emissions in global models to quantify them. We use monthly regional uncertainties of 200 % for DD emissions and monthly global ones of 300 % for SS based on Huneeus et al. (2011) and Textor et al. (2006), respectively. The uncertainties in the monthly regional emission fluxes are combined to provide one on the global-yearly scale and thus ease the comparison

with other results. This global-yearly uncertainty estimate is first computed for each one of the species as the square root of the sum of the regional and monthly squared errors (see Appendix A). The resulting global-yearly uncertainties are 2 % for SO_2, 13 % for BC, 20 % for POM, 26 % for DD and 86 % for SS. These estimates assume no temporal correlation between the uncertainties from one month to the next. However, some dependence in time can be expected and is in fact implicit in the system because of the two-month window of the data assimilation (Huneeus et al., 2012). Temporal correlation in the emission uncertainties could arise from various assumptions made in the preparation of the emission inventory that would affect all months, such as the use of erroneous energy statistics or emission factors. To estimate the impact of this temporal dependency, we recomputed the global-yearly error assuming that the uncertainties between months are fully correlated. The resulting global-yearly uncertainties are then 7 % for SO_2, 40 % for BC, 55 % for POM, 81 % for DD and 300 % for SS. As reality is between these two extreme assumptions (fully correlated and fully uncorrelated temporal uncertainties), we conclude that our regional uncertainties provide realistic estimates of the global-yearly emissions.

We also consider the observation error covariance matrix (**R**) to be diagonal. We acknowledge that correlated errors exist between adjacent pixels because of the dependence of the MODIS algorithm on aerosol microphysics and boundary conditions (Zhang et al., 2008). Yet, three adjustments are made to compensate for not considering these correlations. First we apply the bias correction procedure from Zhang and Reid (2006) that corrects some of the systematic errors. Second, we reduce the observation density by thinning the data (Sect. 2.2) and lastly we inflate the observation errors from 0.05 to 0.1 in AOD over ocean and from 0.1 to 0.2 in AOD over land. The last two actions are empirical adjustments that have proven their effectiveness when inverting CO_2 surface fluxes (Chevallier, 2007). The larger errors over land than over ocean take into account the higher precision of the observations over ocean (Remer et al., 2005). In the **R** matrix, we also include the model and representation error of 0.02 already defined in HCB12. We make the hypothesis that the model error is dominated by the simplifications introduced in SPLA and consequently neglect the errors of the original model it was derived from. In HCB12 the performance of the assimilation system was tested for different model errors and the system continued to result in improvement against observations with a model error as high as 0.5 in AOD.

3 Emission inventories

The reference data source used in this work combines the fossil fuel and industrial emissions of SO_2, BC and POM from Lamarque et al. (2010), biomass burning emissions of SO_2, BC and POM from van der Werf et al. (2010), terpene emissions from Lathière et al. (2006), the daily volcanic emissions from Dentener et al. (2006) and the natural emissions of desert dust (DD), sea salt (SS) and dimethyl sulphide (DMS) as presented in HCB12.

Lamarque et al. (2010), hereafter referred as L10, corresponds to a community effort to include and combine the best available information on global and regional emission inventories at the time it was built. It was created to provide consistent and gridded emissions of reactive gases and aerosols for use in chemistry model simulations and to support the Intergovernmental Panel on Climate Change (IPCC) Fifth Assessment Report (AR5).

In L10 the monthly mean emissions of methane (CH_4), carbon monoxide (CO), nitrogen oxides (NO_x), total and speciated non-methane volatile organic compounds (NMVOCs), ammonia (NH_3), organic carbon (OC), black carbon (BC) and sulphur dioxide (SO_2) are provided at a regular grid of 0.5° in latitude and longitude. These emissions are provided for 12 sectors every 10 yr for the period between 1850 and 2000. Seasonal variations (at the monthly scale) are only included for biomass burning, soil NO_x, ship and aircraft emissions. The anthropogenic emissions of BC and OC are an update of Bond et al. (2007) and Junker and Liousse (2008) while SO_2 emissions combine data from Smith et al. (2011), Environmental Protection Agency from the United States (EPA), Environment Canada and the United Nations Framework Convention on Climate Change (UNFCCC). No smoothing is done to remove potential discontinuities across regional boundaries resulting from the combination of different inventories at the regional scale (Lamarque et al., 2010). In the present work only the fossil fuel and industrial emissions of BC, OC and SO_2 for the year 2000 will be considered. We have updated the original biomass burning inventory GFEDv2 (van der Werf et al., 2006) used in L10 with the more recent version 3 (van der Werf et al., 2010). This later version uses improved satellite data and several modifications to the modelling framework were done, such as explicitly accounting for deforestation and forest degradation and partitioning fire emissions into different categories. This dataset provides daily emissions of SO_2, BC and OC with a resolution of 0.5° in latitude and longitude.

As a priori, we choose to use the anthropogenic emissions representative for the year 2000, instead of available projected emissions for the year 2010. We keep the projections for 2010 for later comparison against our estimated fluxes. In view of the strong interannual variability in the biomass burning emissions (van der Werf et al., 2006) we use emissions corresponding to the simulated year (i.e. 2010) for biomass burning emissions.

Volatile organic compounds (VOC) are represented as terpenes in the model (Huneeus et al., 2009) and their emissions are taken from Lathière et al. (2006). Monthly mean biogenic surface fluxes of isoprene, terpenes, acetone and methanol as well as NO soil emissions are calculated for the period 1983–1995 with the vegetation model ORCHIDEE (Organizing

Carbon Hydrology in Dynamic EcosystEms). Even though the estimated emissions do not correspond to the simulated year and the interannual variability in biogenic emissions is of the order of 10 % in this period (Lathière et al., 2006), we decided to use this dataset in the present work for consistency with the simulations conducted within the framework of the AR5 (Szopa et al., 2012).

The DD emissions are pre-calculated offline at a higher resolution ($1.125° \times 1.125°$) using the 6-hourly horizontal 10 m wind speed from the European Centre for Medium-Range Weather Forecasts (ECMWF) and are then re-gridded to the model resolution while conserving the global flux. For SS we use the formulation of Monahan et al. (1986) as a function of the 10 m wind speed (HCB12).

In addition to the above-described dataset, we explore the sensitivity of the estimated emissions, on one hand by replacing the GFEDv3 biomass burning emissions with the GFAS v1.0 inventory (Kaiser et al., 2012), and on the other hand by replacing the Lamarque et al. (2010) anthropogenic emissions of SO_2, BC and POM with the AeroCom emission inventory of the year 2000 (Diehl et al., 2012). These inventories not only change the regional prior values, but also the prescribed sub-regional and temporal patterns. The differences between the biomass burning inventories and the anthropogenic emissions of SO_2, BC and POM are analysed in Kaiser et al. (2012) and Diehl et al. (2012), respectively.

The GFAS inventory estimates biomass burning emissions by using the FRP observations from the MODIS instrument onboard the Terra and Aqua satellites. It uses the quantitative information on the combustion rate in the FRP and detects fires in real time at high spatial and temporal resolution. We follow the authors' recommendation and apply a global enhancement factor of 3.4 to particulate matter emissions to better match observed aerosol distributions.

The AeroCom inventory corresponds to a compilation of anthropogenic emissions of BC, OC and SO_2 for the period 1980–2010 to facilitate intercomparison of hindcast simulations of aerosols (http://aerocom.met.no/). The BC and OC emissions are based on the gridded inventory for 1996 from Bond et al. (2004) while for SO_2, the emissions are based on the Emissions Database for Global Atmospheric Research release version 4.1 (EDGARv4.1) inventory. This inventory provides SO_2 emissions from 1975 to 2000 every five years and then yearly from 2000 until 2006. For BC and OC, the emissions are updated over the period to account for regional emission trends using data from Streets et al. (2006, 2008, 2009).

The combination of L10, also known as ACCMIP (Emissions for Atmospheric Chemistry and Climate Model Intercomparison Project; Granier et al., 2011), with the GFEDv3 biomass burning emissions will be referred to as ACFED, while the experiment using the combination of ACCMIP and GFAS will be referred to as ACFAS. Finally, the experiments combining AeroCom fossil fuel and industrial emissions and biomass burning of GFED and GFAS will be referred to as AEFED and AEFAS, respectively.

4 Results

We assess the validity and the quality of the estimated emission by examining first the model performance to reproduce the assimilated AOD and an independent AOD dataset (Sect. 4.1). We then analyse the estimated fluxes both in terms of global and regional values, assess their robustness to the choice of the a priori emission inventories and compare them to values from the literature (Sect. 4.2). To finalize, we will present the uncertainties of the estimated fluxes and compare them to values found in the literature (Sect. 4.3). The analysis will be conducted focusing on the ACFED combination of inventories.

We make use of the tools developed at the Laboratoire des Sciences du Climat et de l'Environnement (LSCE) in the framework of the AeroCom project, which includes a platform for detailed evaluation of aerosol simulation in global models (http://aerocom.met.no/).

4.1 Statistical analysis

The first step to validate the estimated fluxes is to assess their ability to improve the simulation of the AOD, with respect to both the assimilated and independent observations. We do so by examining the difference between the first guess (FG) and the analysis (AN) to the observations via the root mean square (RMS) error, mean bias and Pearson correlation coefficient (R). As independent dataset, we use measurements from the AErosol RObotic NETwork (AERONET). This is a global network of more than 300 sun photometers that monitor AOD and aerosol properties under various different atmospheric aerosol loads (Holben et al., 1998, 2001).

Although AERONET also provides instantaneous and daily-averaged AOD data, we shall focus on the monthly values in accordance with the scale of the state vector (Sect. 2.3). We compute the model monthly mean by sampling only those days when AERONET data are available. We use available stations with measurements for the year 2010. Stations above 1000 m a.s.l. are excluded since we do not correct the model AOD for the station altitude. For the analysis with respect to the MODIS data, the model monthly mean is computed using only days and grid boxes when MODIS observations are available.

The assimilation is effective in bringing the simulated AOD closer to MODIS, for both total (Table 1) and fine mode AOD (Table 2), in terms of root mean square error and correlation coefficient. Larger impacts are seen in the total AOD than in the fine mode AOD. For the former the RMS error (correlation coefficient) is reduced (increased) by 21 and 25 %, respectively, whereas for the latter, the RMS error (correlation) is decreased (increased) by 5 and 18 %, respectively.

Table 1. Statistics quantifying the difference in total AOD between the first guess (FG) or analysis (AN) and MODIS or AERONET for all four experiments ACFED, ACFAS, AEFED and AEFAS. For each AERONET station, the closest model grid box is used. The statistics for both, MODIS and AERONET, are computed at the global scale, considering the full yearly cycle.

		Total AOD							
		ACFED		ACFAS		AEFED		AEFAS	
		FG	AN	FG	AN	FG	AN	FG	AN
MODIS	RMS	0.125	0.099	0.122	0.098	0.125	0.099	0.122	0.098
	Mean Bias	−0.053	−0.040	−0.040	−0.039	−0.053	−0.040	−0.039	−0.039
	Correlation	0.576	0.718	0.618	0.724	0.575	0.716	0.619	0.723
AERONET	RMS	0.131	0.103	0.129	0.104	0.131	0.102	0.129	0.102
	Mean Bias	−0.007	−0.003	0.005	−0.002	−0.007	−0.006	0.005	−0.005
	Correlation	0.554	0.736	0.599	0.733	0.556	0.743	0.600	0.742

Table 2. Same as Table 1 but for fine mode AOD.

		Fine Mode AOD							
		ACFED		ACFAS		AEFED		AEFAS	
		FG	AN	FG	AN	FG	AN	FG	AN
MODIS	RMS	0.048	0.046	0.054	0.046	0.049	0.046	0.055	0.046
	Mean Bias	−0.005	0.008	0.002	0.008	−0.005	0.008	0.002	0.008
	Correlation	0.607	0.714	0.647	0.716	0.610	0.709	0.652	0.712
AERONET	RMS	0.112	0.101	0.116	0.102	0.112	0.104	0.116	0.104
	Mean Bias	0.037	0.044	0.050	0.045	0.037	0.041	0.049	0.042
	Correlation	0.556	0.727	0.628	0.725	0.557	0.701	0.628	0.699

However, although the system reduces the bias in the total AOD, it increases it slightly in the fine mode AOD. The same is valid over ocean, where all statistics are improved for the total AOD, whereas for the fine mode AOD the bias is also increased in the AN compared to the FG (not shown). When computing the statistics with respect to AERONET, the same features are observed (Tables 1, 2). Larger improvements are seen in the total AOD than the fine mode AOD. Additionally, the RMS error (correlation coefficient) is decreased (increased) for both total and fine mode AOD, whereas the mean bias is decreased only for the total AOD. The decrease in RMS error for the total AOD with respect to MODIS is observed in all IND regions and all BB regions except Equatorial Asia (EQAS) (Fig. 2). Furthermore, the correlation is also increased in all IND regions while it is increased in all BB regions except EQAS and Temperate North America (TENA). Finally, the bias is increased in the BB regions of Boreal North America (BONA), Inner Asia (INAS), Australia (AUST), TENA, Europe (EURO) and China (CHNA) and in the IND regions of North America (NOAM), North Africa (NOAF), INDIA, East Asia (EAAS) and AUST.

The fine mode AOD is assimilated over ocean only, i.e. in more remote and pristine conditions, and not over continents where large AOD values are observed in polluted regions. Therefore, the fine mode AOD statistics with respect to MODIS also evaluate the transport and removal processes rather than just the emission intensity. However, this argument is not applicable for the bias with respect to AERONET since most of the stations are over land measuring a mix of remote and polluted conditions. Two factors could explain this bias degradation for AERONET (despite betters RMS errors and correlations): a mismatch and representation error between AERONET and MODIS due to the thinning of the latter for their use in the assimilation (HCB12) and the slightly different definition of the aerosol fine mode fraction in the MODIS and AERONET algorithms (Kleidman et al., 2005).

The statistics were computed for the four inversions with different combinations of BB and IND emissions. All in all, the same behaviour as described above is observed in the remaining three experiments, both with respect to MODIS and AERONET (Tables 1, 2). The sole exceptions to the above are the two combinations with GFAS that present a decrease in bias for the fine mode AOD with respect to AERONET.

We highlight that for the total AOD, experiments using GFAS in the a priori emissions have a FG closer to the observations (smaller RMS error and larger correlation) than those using GFED, irrespective of whether the validation is done with respect to MODIS or AERONET. Yet after inversion the analysis in all four experiments presents similar

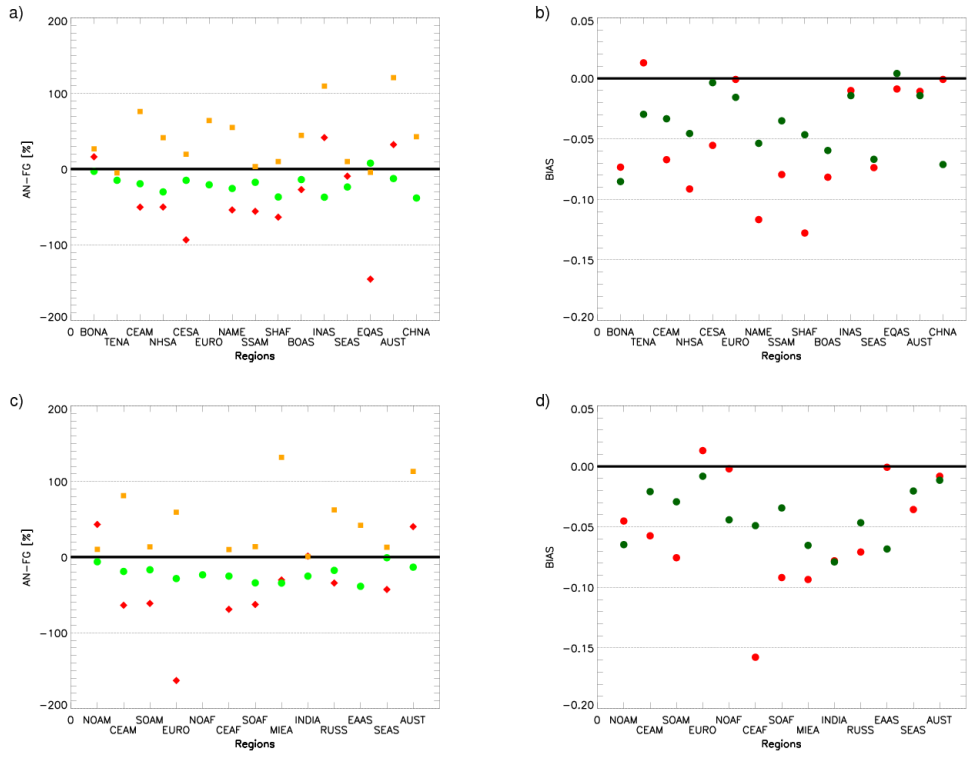

Fig. 2. Total AOD change in RMS error (green circles), mean bias (red diamond) and correlation (orange squares) between FG and AN with respect to MODIS AOD (in %) for **(a)** biomass burning and **(c)** industrial regions identified in the *x* axis. In addition, bias in AOD (unitless) for FG (red) and AN (green) with respect to MODIS for **(b)** biomass burning and **(d)** industrial regions (identified in the *x* axis) are illustrated. Regions are presented in Sect. 2.3 and illustrated in Fig. 1.

statistics, in particular in terms of RMS error. Small differences in bias and correlation can be seen for the AN with respect to AERONET. They suggest that while the statistics of the FG are mostly determined by the BB inventory, the choice of the fossil fuel and industrial inventory determines the statistics of the AN. Likewise for the fine mode AOD, combinations with GFED and GFAS differ in their FG statistics with respect to MODIS but present similar statistics after the inversion with respect to AERONET. The statistics before the inversion seem to be dominated by the BB inventory but by the fossil fuel and industrial inventory after the inversion.

4.2 Emission fluxes

The estimated fluxes for the baseline experiment (i.e. ACFED) are 67 Tg S yr^{-1} for SO_2, 12 Tg yr^{-1} for BC, 87 Tg yr^{-1} for POM, 1206 Tg yr^{-1} for DD and 16850 Tg yr^{-1} for SS (Table 3). Most of the emissions were increased except for DD, which was decreased by 8 % with respect to the FG. The largest increase is in BC (73 %) and POM (72 %) emissions while the smallest is in SS emissions (1 %). The increase in SO_2 emissions is 36 %.

The emissions of SO_2 and BC were increased in all experiments after inversion, yet POM AN emissions for ACFAS and AEFAS were reduced (Table 3). The maximum difference of the three a priori inventories to the reference one was reduced from 11, 57 and 108 % down to 6, 13 and 17 % for SO_2, BC and POM, respectively. For both SS and DD, all four experiments use the same a priori flux and after inversion the emissions from the ACFAS, AEFED and AEFAS experiments present differences with respect to ACFED that do not exceed 2 %.

For anthropogenic and BB emissions, we compare the new emission fluxes (AN) and FG fluxes to the projected emissions for the year 2010 from the Representative Concentration Pathways (RCPs). The RCPs correspond to a total of four harmonized emission scenarios for gaseous and particulate species developed as a basis for long-term and near-term modelling experiments. These four scenarios span the range from 2.6 to 8.5 W m^{-2} radiative forcing values for the year 2100 (van Vuuren et al., 2011) but do not differ much for the year 2010 which is of interest here. We use the RCP 8.5 emissions in this study. To ease the comparison we have converted OC emissions given in L10 and the different RCPs to POM by applying a conversion factor of 1.6 between both species. This is the same method applied in SPLA to convert OC to POM emissions (Huneeus et al., 2009).

We recall that the emissions used as FG correspond to inventory L10 for the year 2000 and were used as starting point

Table 3. Total FG and AN annual emissions in $TgS\,yr^{-1}$ for SO_2 and $Tg\,yr^{-1}$ for the other aerosol species for the year 2010 and each one of the four experiments. For SO_2, BC and POM, only the fluxes of the active variables are provided.

	ACFED		ACFAS		AEFED		AEFAS	
	FG	AN	FG	AN	FG	AN	FG	AN
SO_2	44	67	44	65	50	71	50	70
BC	7	12	11	13	7	13	11	14
POM	51	87	105	102	45	80	100	96
DD	1305	1206	1305	1206	1305	1193	1305	1188
SS	16 612	16 851	16 612	16 820	16 612	16 810	16 612	16 781

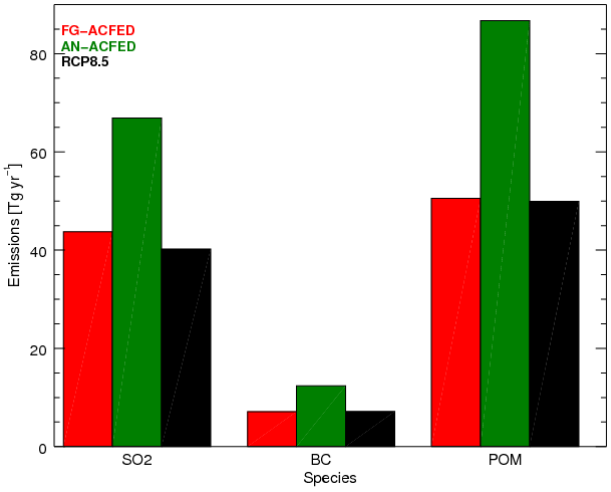

Fig. 3. Global-yearly emissions of SO_2 (in $Tg\,S\,yr^{-1}$), BC and POM (in $Tg\,yr^{-1}$) of FG (red), AN (green) and projected RCP8.5 emissions for the year 2010 (RCP, black). The FG combines the anthropogenic emissions from L10 and the GFED biomass burning emissions.

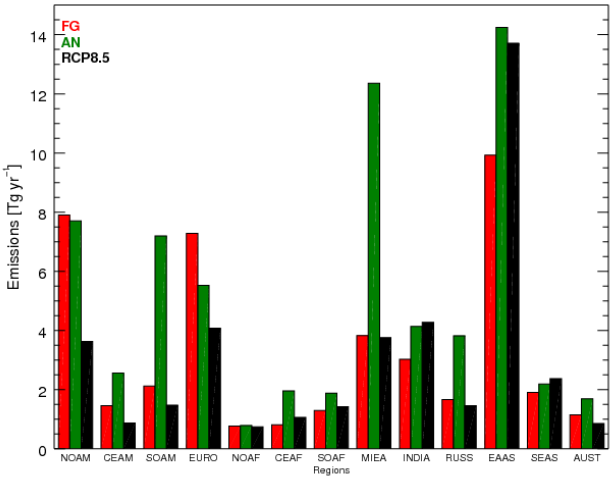

Fig. 4. Same as Fig. 3 but for annual SO_2 emissions in the thirteen regions illustrated in Fig. 1a.

for the RCPs. The RCP8.5 emissions suggest a reduction in the emission of SO_2, BC and POM between the year 2000 and 2010, with a stronger reduction in SO_2 than BC and POM (Fig. 3). The reductions of RCP SO_2 in NOAM and EURO compensate for the increase in INDIA, EAAS and South East Asia (SEAS) (Fig. 4). The assimilation of AOD increases the global-yearly emissions of all three species with stronger increase in SO_2 than POM and BC. Except for North America and Europe where the SO_2 emissions are reduced, they are increased in most regions, with the largest increase in South America, Russia, Middle East and East Asia (Fig. 4). In most regions the SO_2 AN presents larger emissions than both the FG and RCP8.5 increasing the original difference to the RCP8.5 emissions, yet in five regions (NOAM, EURO, INDIA, EAAS and SEAS) the AN reduces this original difference.

The projections for 2010 (RCP8.5) do not present major differences with respect to the FG for BB emissions (Fig. 5b, d) but differences are seen for BC emissions from FF combustion between FG and RCP8.5 in NOAM, South America (SOAM), EURO, INDIA and EAAS which are not present or less important for POM emissions (Fig. 5a, c, respectively). The large increase in BC and POM emissions in the AN (Fig. 3) are dominated by the fluxes in Central Africa (CEAF) as a consequence of combustion of FF (Fig. 5a, c). Additionally, emissions are also increased in India, South Africa and the Middle East. For BB emissions the largest increase in BC and POM are seen in CESA and Southern Hemisphere Africa (SHAF) (Fig. 5b, d). The largest differences of the AN with respect to the projected emissions for 2010 (RCP8.5) coincide with regions where the largest AN increase in emissions is observed. Although the AN emissions mainly increased, a few regions exist where they decreased. For FF combustion the sole regions with reductions are NOAM, EURO and NOAF, with the largest reduction in NOAM, whereas for BB the reductions are in BONA, NAME, SSAM and Boreal Asia (BOAS).

The global estimates for SO_2 and BC are mostly independent of the emission inventory used as FG whereas for POM the choice of the FG influences the final estimate (Fig. 6),

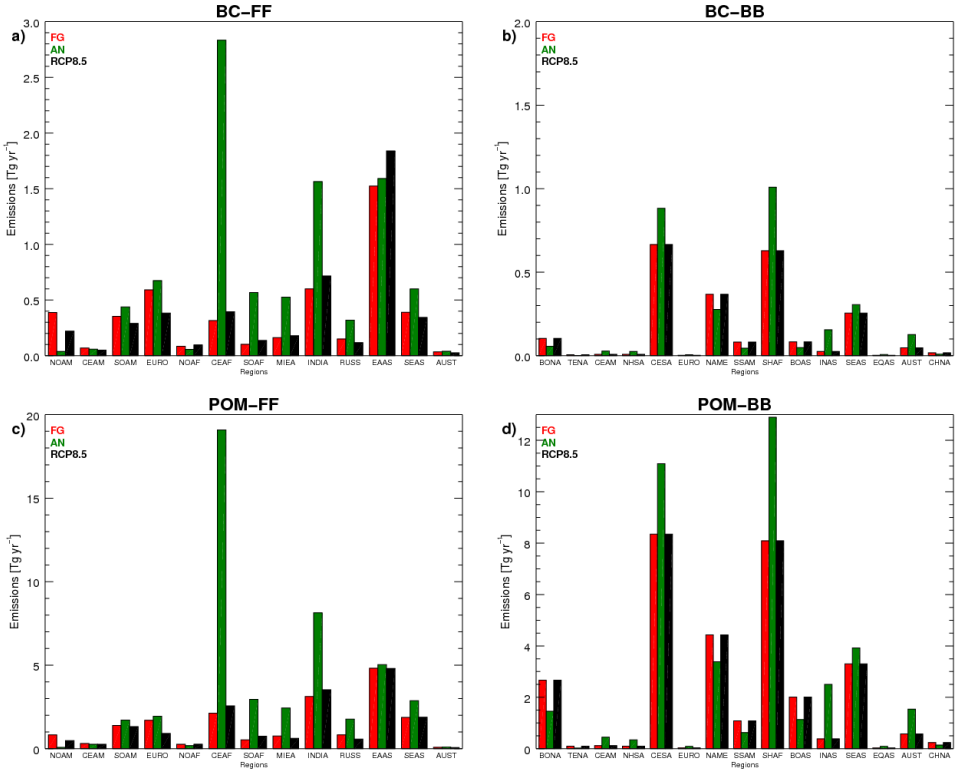

Fig. 5. Same as Fig. 3 but for annual emissions of **(a)** BC and **(c)** POM from FF combustion in the thirteen regions illustrated in Fig. 1a and annual emissions of **(b)** BC and **(d)** POM from BB in the fifteen regions illustrated in Fig. 1b.

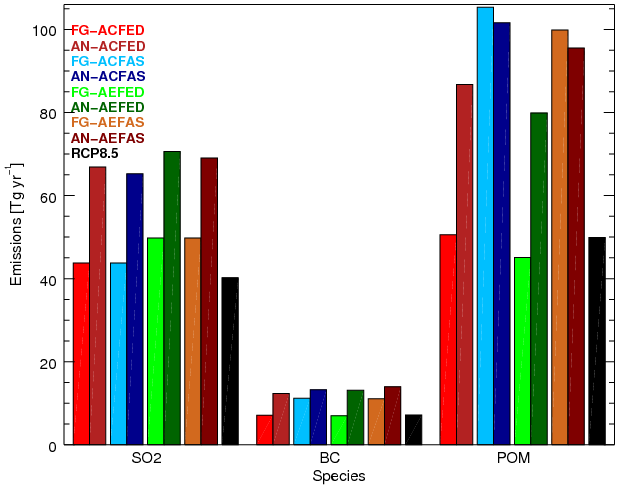

Fig. 6. Global-yearly emissions of SO_2 (in Tg S yr^{-1}), BC and POM (in Tg yr^{-1}) for the FG and AN of the for experiments: ACFED (light and dark red, respectively), ACFAS (light and dark blue, respectively), AEFED (light and dark green, respectively) and AEFAS (light and dark brown, respectively). Projected RCP8.5 emissions for the year 2010 (RCP, black) are also included.

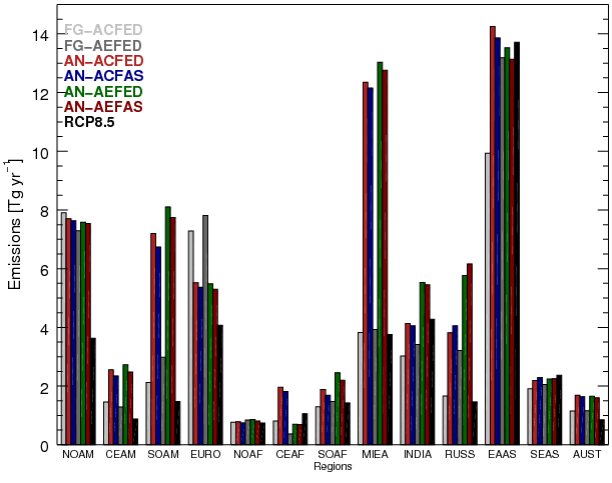

Fig. 7. Annual anthropogenic emissions of SO_2 (in Tg S yr^{-1}) for the FG emissions of the ACFED and AEFED experiments (light and dark grey, respectively) and the AN emissions of the experiments ACFED (red), ACFAS (blue), AEFED (green) and AEFAS (brown). Fluxes are presented for all regions illustrated in Fig. 1a.

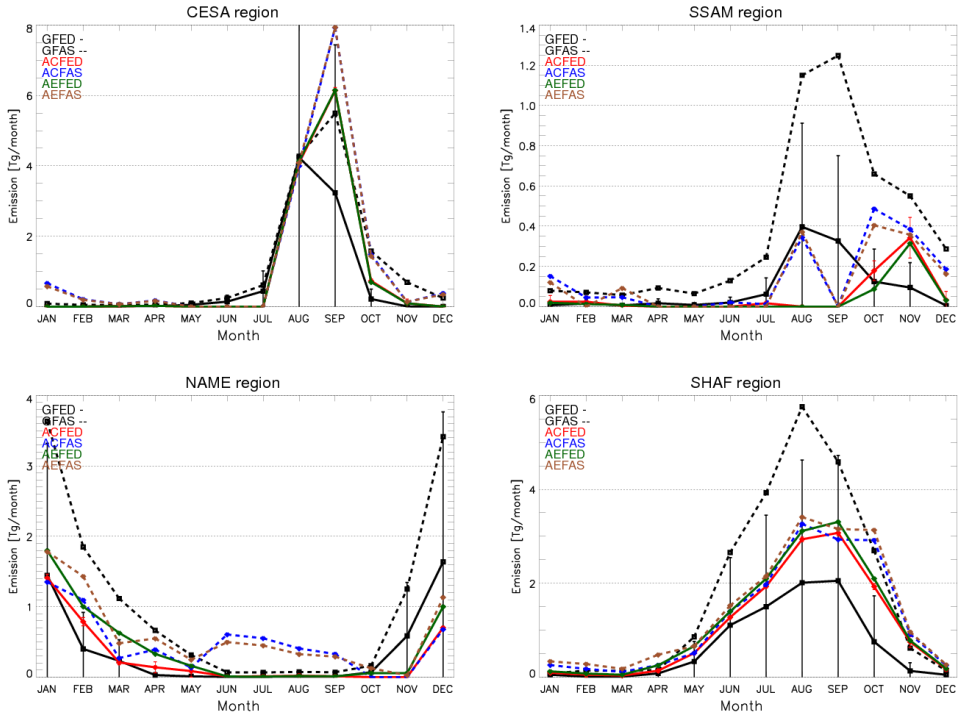

Fig. 8. Seasonal cycle of POM emissions (Tg month^{-1}) from BB in the main four regions illustrated in Fig. 1b. A black solid line illustrates the GFED emissions whereas a black dashed line illustrates the GFAS emissions. The four possible combinations of anthropogenic and biomass burning emission inventories used in this work are included, namely ACFED (red), ACFAS (blue), AEFED (green) and AEFAS (brown). Vertical bars correspond to the uncertainties in the emissions and represent one standard deviation.

mainly due to the choice of BB inventory. On the regional scale however, the choice of the FG has an impact on the estimated fluxes (Figs. 7, 8). For SO_2 the impact of the choice of the first guess depends on the region. While for most regions the differences between the ACCMIP and AeroCom inventories are in general small, there are regions with large discrepancies (Russia (RUSS), CEAF, Southern Africa (SOAF), SOAM and EAAS). After the inversion, these differences are largely reduced except over RUSS, INDIA, CEAF and SOAF where they persist revealing the importance of the choice of the FG (Fig. 7). We assume at this stage that the MODIS AOD are not biased. Sophisticated methods exist to perform bias corrections for the assimilated data but are beyond the scope of this study.

We focus the analysis of the BB emissions to four regions, namely CESA, SSAM, NAME and SHAF. These regions represent approximately 64 % of the BB emissions between 1997 and 2009 (van der Werf et al., 2010). In general both BB inventories present similar seasonal cycles except in SSAM and CESA where the maximum emission from GFAS lags one month behind GFED (Fig. 8). Over SSAM, all four AN emissions coincide with GFAS and have the maximum one month after GFED. In CESA, on the contrary, the emission peak depends on the inventory and differs with both GFED and GFAS. While ACFED and AEFED have the peak in November, ACFAS and AEFAS have it one month before. Important differences exist between both a priori inventories in terms of magnitude, with the largest differences in period of maximum emissions. The behaviour of the four experiments varies from region to region. While in CESA all four AN coincide in presenting larger emissions than both FGs in the month with maximum emissions, in SHAF, on the contrary, the four AN present magnitudes between both FGs throughout most of the year but closer to GFAS from October to December. In NAME the four AN are closer to the GFED inventory except from June to September where ACFAS and AEFAS present significant emissions contrasting with the low emissions of the other inventories. Finally, in SSAM all four AN present magnitudes closer to GFED for the months of April to September, the ACFAS and AEFAS are closer to GFAS for the months of January, March, October and December and the magnitudes of all four AN are between GFED and GFAS for November. The choice of anthropogenic inventory for fossil-fuel emissions used has little impact on the inverted BB emissions; the AN emission time series of the experiments based on GFED have distinguishing features from those based on GFAS. This appears to be a clear improvement brought by our system to existing emission inventories.

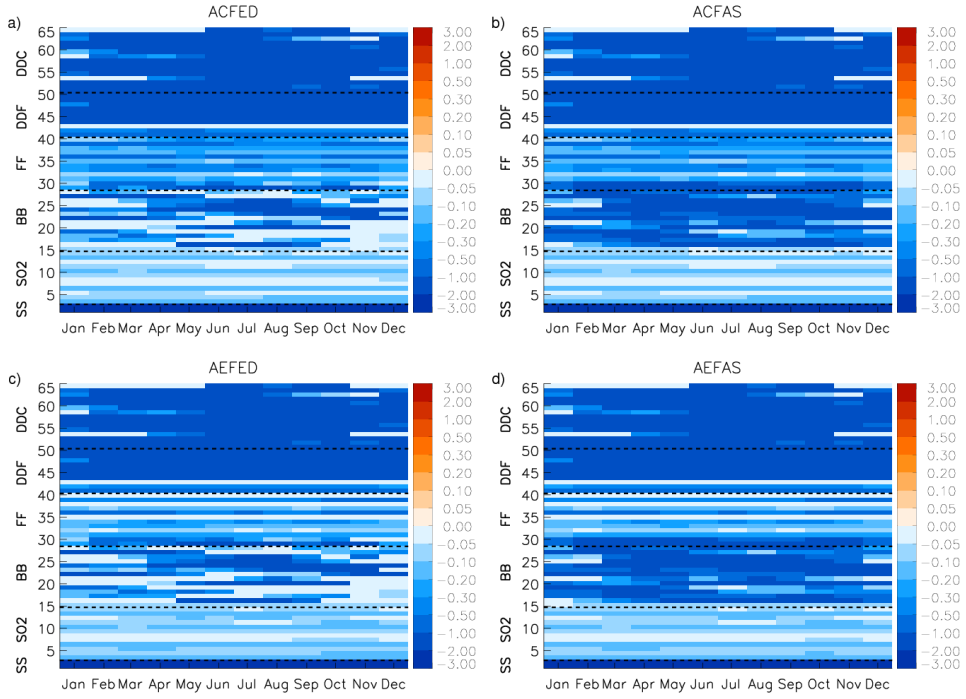

Fig. 9. Difference in monthly mean errors (analysis − first guess) for **(a)** ACFED, **(b)** ACFAS, **(c)** AEFED and **(d)** AEFAS. The number of rows in the figure corresponds to the number of elements in the control vector. Each row corresponds to the seasonal cycle of the difference between analysis and first guess error of a given emission flux and region illustrated in Fig. 1. DDF and DDC correspond to the fine and coarse modes of DD, respectively. The rows between different species are separated by black discontinuous lines. The red/blue colours indicate positive/negative differences.

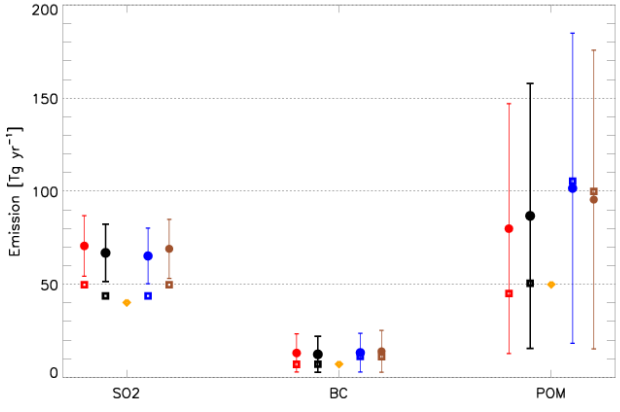

Fig. 10. Global-yearly FG (squares) and AN (circles) emissions of SO_2 (in Tg S yr^{-1}), BC and POM (in Tg yr^{-1}) from experiments ACFED (black), ACFAS (blue), AEFED (red) and AEFAS (brown) for the year 2010. Vertical lines correspond to uncertainties of the corresponding fluxes. Projected RCP emissions are also illustrated (diamond gold). Uncertainties correspond to two standard deviations.

The estimated DD emission of 1206 Tg yr^{-1} from the reference set-up (ACFED) is close to the estimated flux of 1223 Tg yr^{-1} in Ginoux et al. (2012), within the range of emission in global models given in Zender et al. (2004) and Huneeus et al. (2011) and within the estimated emission range in Cakmur et al. (2006). The emissions over both Saharan regions and Saudi Arabia present large increase in DD emissions, yet they do not exceed the decrease observed in East and West Asia, India and North West America (not shown). The FG and AN SS emissions are close to the AeroCom mean of 15 global models (Textor et al., 2006) but exceed by a factor of three the values given in Lewis and Schwartz (2004) and Jaeglé et al. (2011).

4.3 Emission uncertainties

The uncertainty of the estimated emission fluxes or analysis (**A**) can be estimated theoretically at the monthly regional scale by combining the observation and model errors in **R**, weighted by the sensitivities of the AOD to the emissions in the linear operator **H**, with the a priori errors **B** in the following way (Bouttier and Courtier, 1999):

$$A = (\mathbf{H}^{\mathrm{T}}\mathbf{R}^{-1}\mathbf{H} + \mathbf{B}^{-1})^{-1} \,. \quad (3)$$

The initial monthly errors attributed to the FG were assumed to be the same in all regions and throughout the year and were defined as 18 % for SO_2, 130 % for BB, 90 % for FF, 200 % for DD and 300 % for SS (see Sect. 2.4). The analysis errors however, vary throughout the regions and the year. This variability in the error, both in space and time, is introduced by the sensitivities in the linear operator **H**. The regional monthly errors vary between 3 and 18 % for SO_2, 1 and 130 % for BB, 21 and 90 % for FF, 1 and 200 % for DD and 1 and 5 % for SS. The monthly errors are reduced with respect to the FG in all regions and throughout the year for SO_2 and all aerosol species, with the largest reduction for SS (Fig. 9a). This stronger reduction for SS is because the fine mode is assimilated over ocean in addition to the total AOD to constrain the SS emissions. The large upper bound for BB and DD corresponds to regions and months without or small emissions.

The four experiments present similar general features in the seasonal variability of the error reduction (Fig. 9). All experiments agree in presenting the largest reductions for SS and DD for all regions and throughout the year and the smallest ones for SO_2. On the contrary, the intra-annual variability of the error reduction for FF and BB depends on the FG. For FF, ACFED and ACFAS present in general larger relative reductions (and therefore smaller relative AN errors) than AEFED and AEFAS, while for BB, ACFAS and AEFAS present in general larger reductions than ACFED and ACFAS.

The annual global errors are now computed for both the initial errors (**B**) and the errors (**A**) of the AN. The spatial covariance in errors between different species and/or regions as given in the **A** matrix are considered. The temporal correlations between months along the year are not assigned in the inversion system (see Sect. 2.4). In order to account for possible temporal correlation in the annual errors, we compute the global-yearly errors for the case of fully uncorrelated errors and fully correlated ones considering that reality is somewhere in between. The global-yearly errors (with temporal dependance) for the AN are 3 % for SO_2, 14 % for BC, 11 % for POM, 14 % for DD and 2 % for SS. These ranges represent a decrease compared to the global-yearly errors from the FG (7 % for SO_2, 40 % for BC, 55 % for POM, 81 % for DD and 300 % for SS). As for the monthly regional errors, the largest reduction is seen for SS and the smallest one for SO_2 which is almost negligible.

The global-yearly AN fluxes of SO_2, BC and POM of each experiment are all within the uncertainty not only of the corresponding reference flux, but also of the remaining experiments; the spread between the fluxes of the different experiments is smaller than the smallest uncertainty range of the four experiments (Fig. 10). We highlight that in the present analysis the error bars correspond to two standard deviations and therefore represent about 95 % of the uncertainty. Contrary to BC and POM, the SO_2 FG fluxes are outside the uncertainty range of their corresponding AN flux. Likewise, the estimated RCP emissions are within the uncertainty range of the corresponding AN flux from the different experiments, except for SO_2. Although this result suggests that the difference in the SO_2 fluxes is significant, we cannot state at this point whether this difference is due to FG or the projection of the emissions.

5 Conclusions

Aerosols play an important role in air quality, atmospheric visibility, climate and tropospheric chemistry. At present, they represent the largest source of uncertainty when estimating the total anthropogenic radiative forcing of climate, partly due to a lack of knowledge on the spatial and temporal distribution of aerosol emissions. Such knowledge is needed to quantify the impact of aerosols on climate and air quality in regional and global aerosol models.

We have presented a top-down emission inventory for SO_2 and the main aerosol species, namely DD, SS, BC and POM. Monthly mean emissions for the year 2010 were generated by assimilating total and fine mode MODIS AOD at 550 nm into an aerosol model of intermediate complexity. Aerosol emissions are increased or decreased homogenously for each aerosol species and gaseous precursor over a set of predefined regions. These fluxes represent the best compromise between the assimilated observations and the available a priori information on the emissions. The ACCMIP fossil fuel and industrial emissions of SO_2, BC and POM and the GFEDv3 biomass burning emissions of SO_2, BC and POM are used as a priori emissions in the baseline inversion. The sensitivity and robustness of the inversion system to the choice of the a priori emission inventory is investigated by using different combinations of the ACCMIP and AeroCom fossil fuel and industrial and the GFED and GFAS biomass burning sources.

The improvement to the model performance of the new fluxes with respect to the first guess is assessed through the root mean square error, bias and correlation coefficient against the assimilated observations and a set of independent ground-based observations. The resulting aerosol emissions from the four experiments improve all statistics for the total AOD with respect to both sources of observations. For the fine mode AOD, however, while the RMS error (correlation) is decreased (increased), the bias is slightly increased. The absence of fine mode AOD over the continents where the largest AOD occur and the low bias of the FG may explain this feature. Yet this suggests prospect for improvement if fine mode AOD over continent is included in the assimilation. Furthermore, while the FG statistics are determined by the BB inventories, the AN statistics are determined by the fossil fuel and industrial inventories. In addition, the spread in statistics before the inversion is reduced after assimilation of total and fine mode AOD.

The estimated fluxes for the reference experiment (ACFED) were increased by 53, 73, 72 and 1 % for SO_2,

Table 4. Regional-monthly emission errors in % for the FG and the range of AN errors between the four experiments.

	Regional-Monthly	
	FG	AN
SO_2	18	3–18
BB	130	1–130
FF	90	21–90
DD	200	1–200
SS	300	1–5

Table 5. Global-yearly emission errors with temporal dependence in % for the FG and the AN.

	Global-Yearly	
	FG	AN
SO_2	7	3
BC	40	14
POM	55	11
DD	81	14
SS	300	2

BC, POM and SS, respectively, and decreased by 8 % for DD with respect to the a priori values (Table 3). The maximum difference between each one of the three a priori inventories with respect to the reference one was reduced from 11, 57 and 108 % before the inversion, to 6, 13 and 17 % after the inversion, for SO_2, BC and POM, respectively. The resulting baseline emissions were compared to the RCP projected emissions for 2010 for SO_2, BC and POM. At the global scale, the AN presents larger emissions than the RCP for all three species, with larger differences for SO_2 than POM and BC. There are regions however, where the initial difference to the RCP is reduced after inversion. The RCP emissions of SO_2, BC and POM are in general not within the uncertainty range of any of the corresponding AN flux from the four experiments. We cannot determine at this point if this suggests a too conservative emission projection for these species. On the global scale the AN is sensitive on the choice of the BB inventory and not so much on the fossil fuel and industrial inventory. Yet there are regions (RUSS, INDIA, CEAF and SOAF) where the choice of the FG is relevant.

The same FG in the four experiments was used for natural emissions of DD and SS and the combination of fossil fuel and industrial and BB inventory had little if any impact on the final estimated emissions; the differences with respect to the reference flux after the inversion did not exceed 2 %. The estimated emissions of DD are within the range of emissions used in global model and are close to the estimate of Ginoux et al. (2012). The SS AN flux, although within the range of emissions used in the AeroCom global models, differs largely with other estimates found in the literature.

The regional-monthly analysis errors are reduced for all species and throughout the year with respect to the initial values (Table 4). The global-yearly errors were computed with the above values and the impact of a temporal dependence was explored. The errors for the AN were decreased when contrasted to the global-yearly errors from the FG (Table 5). The largest error reduction, both monthly and yearly, is seen for SS and the smallest one for SO_2. The estimated emission fluxes for SO_2, BC and POM are within the uncertainties of the four experiments. The projected SO_2 RCP emissions however, are outside the AN uncertainties of the different setups tested. It is unclear at this point whether this is due to the a priori emission inventories or to projections which are too conservative.

The general validity of the resulting emission fluxes depends also on the aerosol model used in the inversion. The representation of processes such as the formation of secondary aerosols and the aging of particles could lead to biases in the estimated fluxes. To explore the impact of these representations on the resulting emissions, they need to be used in models with higher complexity. The posterior validation of the simulated AOD could reveal weaknesses in the simplification of the aerosol model that will require improvement in the future.

Appendix A

Regional monthly errors are directly available for the background and for the analysis, but in many applications the global-yearly errors are needed. The method to compute the global-yearly errors for a given species is presented here. We take the example of the analysis, but the method applies for the background errors as well.

The first step is to compute the global monthly errors. To do so, we extract for each month t a sub-matrix $\mathbf{A}_t$ of the full analysis error covariance matrix with the relevant elements for a given species. The matrix $\mathbf{A}_t$ contains the variances and covariances in terms of the relative errors, but the operations to aggregate the errors are done in terms of absolute errors. Let $\mathbf{A'}_t$ be the corresponding error covariance matrix in absolute terms for month t. The standard deviation of the global monthly flux for month t (M_t) can be calculated as the square root of the sum of all elements in $\mathbf{A'}_t$.

To compute the global-yearly error, a 12×12 matrix $\mathbf{G}$ is constructed:

$$\mathbf{G}=\begin{pmatrix} M_1 & & & \\ & M_2 & \cdots & \mathrm{cov}(M_j, M_i) \\ & \ddots & & \\ & \mathrm{cov}(M_i, M_j) & \ddots & \\ & & & M_{12} \end{pmatrix}. \quad \text{(A1)}$$

The diagonal terms M_i correspond to the global monthly error computed as described above. The off-diagonal terms $\mathrm{cov}(M_i, M_j)$ correspond to the temporal dependence in the emission errors and are not estimated by the inversion system. The following equation is used to compute this temporal dependence:

$$R_{ij} = \frac{\mathrm{cov}(M_i, M_j)}{\sqrt{M_i}\sqrt{M_j}}. \quad \text{(A2)}$$

The covariance terms $\mathrm{cov}(M_i, M_j)$ $(i \neq j)$ between the global monthly error M_i and M_j are therefore the product of the standard deviation of these errors and of the corresponding correlation coefficient. The global-yearly error is the square root of the sum of the elements in **G**. The range of this error (given by time-uncorrelated and fully time-correlated errors) corresponds to covariance terms computed with correlation coefficients (R_{ij}) equal to zero and 1, respectively.

This principle is valid for the global-yearly error of a single species such as SO_2 or the BC emissions of biomass burning. The same method is applied to compute the global-yearly errors of total BC emissions (i.e., from biomass burning and fossil fuel combustion). The only difference is the size of the matrix **A'** that in addition to including the variances and covariances associated to biomass burning and combustion of fossil fuel, also includes the covariances between the two emission sources.

Acknowledgements. This study was co-funded by the European Commission under the EU Seventh Research Framework Programme (grant agreement No. 283576, MACC II) and the French Ministère de l'Ecologie, du Développement Durable, des Transports et du Logement (MEDDE) under the GMES-MDD programme. The authors are grateful to Michael Schulz for assistance and help in the use of the AeroCom model evaluation tool. The authors would also thank Philippe Bousquet for providing the meteorological fields necessary for the inversion. We also thank the AERONET project at the NASA/GSFC for providing the ground-based aerosol data.

Edited by: W. Lahoz

The publication of this article is financed by CNRS-INSU.

References

Alfaro, S. C., Rajot, J. L., and Nickling, W.: Estimation of PM_{20} emissions by wind erosion: main sources of uncertainties, Geomorphology, 59, 63–74, 2004.

Assamoi, E.-M. and Liousse, C.: A new inventory for two-wheel vehicle emissions in West Africa for 2002, Atmos. Environ., 44, 3985–3996, doi:10.1016/j.atmosenv.2010.06.048, 2010.

Bauer, S. E., Balkanski, Y., Schulz, M., Hauglustaine, D. A., and Dentener, F.: Global modeling of heterogeneous chemistry on mineral aerosol surfaces: influence on tropospheric ozone chemistry and comparison to observations, J. Geophys. Res.-Atmos., 109, D02304, doi:10.1029/2003jd003868, 2004.

Bond, T. C., Streets, D. G., Yarber, K. F., Nelson, S. M., Woo, J.-H., and Klimont, Z.: A technology-based global inventory of black and organic carbon emissions from combustion, J. Geophys. Res.: Atmos., 109, 1–43, doi:10.1029/2003jd003697, 2004.

Bond, T. C., Bhardwaj, E., Dong, R., Jogani, R., Jung, S., Roden, C., Streets, D. G., and Trautmann, N. M.: Historical emissions of black and organic carbon aerosol from energy-related combustion, 1850–2000, Global Biogeochem. Cy., 21, GB2018, doi:10.1029/2006gb002840, 2007.

Bouttier, F. and Courtier, C.: Data assimilation methods and concepts, Meteorological Training Course Lecture Series, European Centre for Medium Range Weather Forecast, 59 pp., 1999.

Cakmur, R. V., Miller, R. L., Perlwitz, J., Geogdzhayev, I. V., Ginoux, P., Koch, D., Kohfeld, K. E., Tegen, I., and Zender, C. S.: Constraining the magnitude of the global dust cycle by minimizing the difference between a model and observations, J. Geophys. Res.: Atmos., 111, 1–24, doi:10.1029/2005jd005791, 2006.

Chevallier, F.: Impact of correlated observation errors on inverted CO_2 surface fluxes from OCO measurements, Geophys. Res. Lett., 34, 1–6, doi:10.1029/2007gl030463, 2007.

Chevallier, F., Fisher, M., Peylin, P., Serrar, S., Bousquet, P., Bréon, F. M., Chédin, A., and Ciais, P.: Inferring CO_2 sources and sinks from satellite observations: method and application to TOVS data, J. Geophys. Res., 110, D24309, doi:10.1029/2005jd006390, 2005.

de Leeuw, G., Andreas, E. L., Anguelova, M. D., Fairall, C. W., Lewis, E. R., O'Dowd, C., Schulz, M., and Schwartz, S. E.: Production flux of sea spray aerosol, Rev. Geophys., 49, 1–39, doi:10.1029/2010rg000349, 2011.

Denman, K. L., Brasseur, G., Chidthaisong, A., Ciais, P., Cox, P. M., Dickinson, R. E., Hauglustaine, D., Heinze, C., Holland, E., Jacob, D., Lohmann, U., Ramachandran, S., da Silva Dias, P. L., Wofsy, S. C., and Zhang, X.: Couplings between changes in the climate system and biogeochemistry, in: Climate Change 2007: The Physical Science Basis. Contribution of Working Group I to the Fourth Assessment Report of the Intergovernmental Panel on Climate Change, edited by: Solomon, S., Qin, D., Manning, M., Chen, Z., Marquis, M., Averyt, K. B., Tignor, M., and Miller, H. L., Cambridge University Press, Cambridge, UK and New York, NY, USA, 2007.

Dentener, F., Kinne, S., Bond, T., Boucher, O., Cofala, J., Generoso, S., Ginoux, P., Gong, S., Hoelzemann, J. J., Ito, A., Marelli, L., Penner, J. E., Putaud, J.-P., Textor, C., Schulz, M., van der Werf, G. R., and Wilson, J.: Emissions of primary aerosol and precursor gases in the years 2000 and 1750 prescribed data-sets for AeroCom, Atmos. Chem. Phys., 6, 4321–4344, doi:10.5194/acp-6-4321-2006, 2006.

Diehl, T., Heil, A., Chin, M., Pan, X., Streets, D., Schultz, M., and Kinne, S.: Anthropogenic, biomass burning, and volcanic emissions of black carbon, organic carbon, and SO_2 from 1980 to 2010 for hindcast model experiments, Atmos. Chem. Phys. Discuss., 12, 24895–24954, doi:10.5194/acpd-12-24895-2012, 2012.

Dubovik, O., Lapyonok, T., Kaufman, Y. J., Chin, M., Ginoux, P., Kahn, R. A., and Sinyuk, A.: Retrieving global aerosol sources from satellites using inverse modeling, Atmos. Chem. Phys., 8, 209–250, doi:10.5194/acp-8-209-2008, 2008.

Eyring, V., Isaksen, I. S. A., Berntsen, T., Collins, W. J., Corbett, J. J., Endresen, O., Grainger, R. G., Moldanova, J., Schlager, H., and Stevenson, D. S.: Transport impacts on atmosphere and climate: shipping, Atmos. Environ., 44, 4735–4771, doi:10.1016/j.atmosenv.2009.04.059, 2010.

Forster, P., Ramaswamy, V., Artaxo, P., Berntsen, T., Betts, R., Fahey, D. W., Haywood, J., Lean, J., Lowe, D. C., Myhre, G., Nganga, J., Prinn, R., Raga, G., Schulz, M., and Van Dorland, R.: Changes in atmospheric constituents and in radiative forcing, in: Climate Change 2007: The Physical Science Basis. Contribution of Working Group I to the Fourth Assessment Report of the Intergovernmental Panel on Climate Change, edited by: Solomon, S., Qin, D., Manning, M., Chen, Z., Marquis, M., Averyt, K. B., Tignor, M., and Miller, H. L., Cambridge University Press, Cambridge, UK and New York, NY, USA, 2007.

Fu, T. M., Cao, J. J., Zhang, X. Y., Lee, S. C., Zhang, Q., Han, Y. M., Qu, W. J., Han, Z., Zhang, R., Wang, Y. X., Chen, D., and Henze, D. K.: Carbonaceous aerosols in China: top-down constraints on primary sources and estimation of secondary contribution, Atmos. Chem. Phys., 12, 2725–2746, doi:10.5194/acp-12-2725-2012, 2012.

Generoso, S., Bréon, F. M., Balkanski, Y., Boucher, O., and Schulz, M.: Improving the seasonal cycle and interannual variations of biomass burning aerosol sources, Atmos. Chem. Phys., 3, 1211–1222, doi:10.5194/acp-3-1211-2003, 2003.

Ginoux, P., Chin, M., Tegen, I., Prospero, J. M., Holben, B., Dubovik, O., and Lin, S. J.: Sources and distributions of dust aerosols simulated with the GOCART model, J. Geophys. Res.-Atmos., 106, 20255–20273, 2001.

Ginoux, P., Prospero, J. M., Gill, T. E., Hsu, N. C., and Zhao, M.: Global-scale attribution of anthropogenic and natural dust sources and their emission rates based on MODIS Deep Blue aerosol products, Rev. Geophys., 50, 1–36, doi:10.1029/2012rg000388, 2012.

Granier, C., Bessagnet, B., Bond, T., D'Angiola, A., van der Gon, H. D., Frost, G. J., Heil, A., Kaiser, J. W., Kinne, S., Klimont, Z., Kloster, S., Lamarque, J.-F., Liousse, C., Masui, T., Meleux, F., Mieville, A., Ohara, T., Raut, J.-C., Riahi, K., Schultz, M. G., Smith, S. J., Thompson, A., van Aardenne, J., van der Werf, G. R., van Vuuren, D. P.: Evolution of anthropogenic and biomass burning emissions of air pollutants at global and regional scales during the 1980–2010 period, Clim. Change, 109, 163–190, doi:10.1007/s10584-011-0154-1, 2011.

Hakami, A., Henze, D. K., Seinfeld, J. H., Chai, T., Tang, Y., Carmichael, G. R., and Sandu, A.: Adjoint inverse modeling of black carbon during the Asian Pacific Regional Aerosol Characterization Experiment, J. Geophys. Res.-Atmos., 110, D14301, doi:10.1029/2004jd005671, 2005.

Haywood, J. and Boucher, O.: Estimates of the direct and indirect radiative forcing due to tropospheric aerosols: a review, Rev. Geophys., 38, 513–543, doi:10.1029/1999rg000078, 2000.

Haywood, J. and Schulz, M.: Causes of the reduction in uncertainty in the anthropogenic radiative forcing of climate between IPCC (2001) and IPCC (2007), Geophys. Res. Lett., 34, L20701, doi:10.1029/2007gl030749, 2007.

Hoelzemann, J. J., Schultz, M. G., Brasseur, G. P., Granier, C., and Simon, M.: Global Wildland Fire Emission Model (GWEM): evaluating the use of global area burnt satellite data, J. Geophys. Res.-Atmos., 109, D14S04, doi:10.1029/2003jd003666, 2004.

Holben, B. N., Eck, T. F., Slutsker, I., Tanre, D., Buis, J. P., Setzer, A., Vermote, E., Reagan, J. A., Kaufman, Y. J., Nakajima, T., Lavenu, F., Jankowiak, I., and Smirnov, A.: AERONET – a federated instrument network and data archive for aerosol characterization, Remote Sens. Environ., 66, 1–16, 1998.

Holben, B. N., Tanre, D., Smirnov, A., Eck, T. F., Slutsker, I., Abuhassan, N., Newcomb, W. W., Schafer, J. S., Chatenet, B., Lavenu, F., Kaufman, Y. J., Castle, J. V., Setzer, A., Markham, B., Clark, D., Frouin, R., Halthore, R., Karneli, A., O'Neill, N. T., Pietras, C., Pinker, R. T., Voss, K., and Zibordi, G.: An emerging ground-based aerosol climatology: aerosol optical depth from AERONET, J. Geophys. Res.-Atmos., 106, 12067–12097, 2001.

Hubanks, P. A., King, M. D., Platnick, S., and Pincus, R.: MODIS Atmosphere L3 Gridded Product Algorithm Theoretical Basis-Document, 96 pp., 2008.

Huneeus, N., Boucher, O., and Chevallier, F.: Simplified aerosol modeling for variational data assimilation, Geosci. Model Dev., 2, 213–229, doi:10.5194/gmd-2-213-2009, 2009.

Huneeus, N., Schulz, M., Balkanski, Y., Griesfeller, J., Prospero, J., Kinne, S., Bauer, S., Boucher, O., Chin, M., Dentener, F., Diehl, T., Easter, R., Fillmore, D., Ghan, S., Ginoux, P., Grini, A., Horowitz, L., Koch, D., Krol, M. C., Landing, W., Liu, X., Mahowald, N., Miller, R., Morcrette, J.-J., Myhre, G., Penner, J., Perlwitz, J., Stier, P., Takemura, T., and Zender, C. S.: Global dust model intercomparison in AeroCom phase I, Atmos. Chem. Phys., 11, 7781–7816, doi:10.5194/acp-11-7781-2011, 2011.

Huneeus, N., Chevallier, F., and Boucher, O.: Estimating aerosol emissions by assimilating observed aerosol optical depth in a global aerosol model, Atmos. Chem. Phys., 12, 4585–4606, doi:10.5194/acp-12-4585-2012, 2012.

Ito, A. and Penner, J. E.: Historical emissions of carbonaceous aerosols from biomass and fossil fuel burning for the period 1870–2000, Global Biogeochem. Cy., 19, 1–14, doi:10.1029/2004gb002374, 2005.

Jaeglé, L., Quinn, P. K., Bates, T. S., Alexander, B., and Lin, J. T.: Global distribution of sea salt aerosols: new constraints from in situ and remote sensing observations, Atmos. Chem. Phys., 11, 3137–3157, doi:10.5194/acp-11-3137-2011, 2011.

Junker, C. and Liousse, C.: A global emission inventory of carbonaceous aerosol from historic records of fossil fuel and biofuel consumption for the period 1860–1997, Atmos. Chem. Phys., 8, 1195–1207, doi:10.5194/acp-8-1195-2008, 2008.

Kaiser, J. W., Heil, A., Andreae, M. O., Benedetti, A., Chubarova, N., Jones, L., Morcrette, J. J., Razinger, M., Schultz, M. G., Suttie, M., and van der Werf, G. R.: Biomass burning emissions estimated with a global fire assimilation system based on observed fire radiative power, Biogeosciences, 9, 527–554, doi:10.5194/bg-9-527-2012, 2012.

Keuken, M., Zandveld, P., van den Elshout, S., Janssen, N. A. H., and Hoek, G.: Air quality and health impact of PM_{10} and EC in the city of Rotterdam, the Netherlands in 1985–2008, Atmos. Environ., 45, 5294–5301, doi:10.1016/j.atmosenv.2011.06.058, 2011.

King, M. D., Menzel, W. P., Kaufman, Y. J., Tanre, D., Gao, B. C., Platnick, S., Ackerman, S. A., Remer, L. A., Pincus, R., and

Hubanks, P. A.: Cloud and aerosol properties, precipitable water, and profiles of temperature and water vapor from MODIS, IEEE T. Geosci. Remote, 41, 442–458, 2003.

Kleidman, R. G., O'Neill, N. T., Remer, L. A., Kaufman, Y. J., Eck, T. F., Tanré, D., Dubovik, O., and Holben, B. N.: Comparison of Moderate Resolution Imaging Spectroradiometer (MODIS) and Aerosol Robotic Network (AERONET) remote-sensing retrievals of aerosol fine mode fraction over ocean, J. Geophys. Res.-Atmos., 110, 1–6, doi:10.1029/2005jd005760, 2005.

Lamarque, J.-F., Bond, T. C., Eyring, V., Granier, C., Heil, A., Klimont, Z., Lee, D., Liousse, C., Mieville, A., Owen, B., Schultz, M. G., Shindell, D., Smith, S. J., Stehfest, E., Van Aardenne, J., Cooper, O. R., Kainuma, M., Mahowald, N., McConnell, J. R., Naik, V., Riahi, K., and van Vuuren, D. P.: Historical (1850–2000) gridded anthropogenic and biomass burning emissions of reactive gases and aerosols: methodology and application, Atmos. Chem. Phys., 10, 7017–7039, doi:10.5194/acp-10-7017-2010, 2010.

Lathière, J., Hauglustaine, D. A., Friend, A. D., De Noblet-Ducoudré, N., Viovy, N., and Folberth, G. A.: Impact of climate variability and land use changes on global biogenic volatile organic compound emissions, Atmos. Chem. Phys., 6, 2129–2146, doi:10.5194/acp-6-2129-2006, 2006.

Laurent, B., Marticorena, B., Bergametti, G., Léon, J. F., and Mahowald, N. M.: Modeling mineral dust emissions from the Sahara desert using new surface properties and soil database, J. Geophys. Res.: Atmos., 113, 1–20, doi:10.1029/2007jd009484, 2008.

Lee, L. A., Carslaw, K. S., Pringle, K. J., Mann, G. W., and Spracklen, D. V.: Emulation of a complex global aerosol model to quantify sensitivity to uncertain parameters, Atmos. Chem. Phys., 11, 12253–12273, doi:10.5194/acp-11-12253-2011, 2011.

Lei, Y., Zhang, Q., He, K. B., and Streets, D. G.: Primary anthropogenic aerosol emission trends for China, 1990–2005, Atmos. Chem. Phys., 11, 931–954, doi:10.5194/acp-11-931-2011, 2011.

Lewis, E. R. and Schwartz, S. E.: Sea Salt Aerosol Production: Mechanisms, Methods, Measurements, and Models: A Critical Review, American Geophysical Union, Washington, DC, 2004.

Lu, Z., Streets, D. G., Zhang, Q., Wang, S., Carmichael, G. R., Cheng, Y. F., Wei, C., Chin, M., Diehl, T., and Tan, Q.: Sulfur dioxide emissions in China and sulfur trends in East Asia since 2000, Atmos. Chem. Phys., 10, 6311–6331, doi:10.5194/acp-10-6311-2010, 2010.

Lu, Z., Zhang, Q., and Streets, D. G.: Sulfur dioxide and primary carbonaceous aerosol emissions in China and India, 1996–2010, Atmos. Chem. Phys., 11, 9839–9864, doi:10.5194/acp-11-9839-2011, 2011.

Marticorena, B., Chazette, P., Bergametti, G., Dulac, F., and Legrand, M.: Mapping the aerodynamic roughness length of desert surfaces from the POLDER/ADEOS bi-directional reflectance product, Int. J. Remote Sens., 25, 603–626, doi:10.1080/0143116031000116976, 2004.

Monahan, E. C., Spliel, D. E., and Davidson, K. L.: A models of marine aerosol generation via whitecaps and wave disruption, in: Oceanic Whitecaps, edited by: Monahan, E. C. and Mac Niocail, G., Springer, New York, 167–174, 1986.

O'Dowd, C. D., Smith, M. H., Consterdine, I. E., and Lowe, J. A.: Marine aerosol, sea-salt, and the marine sulphur cycle: a short review, Atmos. Environ., 31, 73–80, 1997.

Ohara, T., Akimoto, H., Kurokawa, J., Horii, N., Yamaji, K., Yan, X., and Hayasaka, T.: An Asian emission inventory of anthropogenic emission sources for the period 1980–2020, Atmos. Chem. Phys., 7, 4419–4444, doi:10.5194/acp-7-4419-2007, 2007.

Olivier, J. G. J., Van Aardenne, J. A., Dentener, F. J., Pagliari, V., Ganzeveld, L. N., and Peters, J. A. H. W.: Recent trends in global greenhouse gas emissions: regional trends 1970–2000 and spatial distributionof key sources in 2000, Environ. Sci., 2, 81–99, doi:10.1080/15693430500400345, 2005.

Pérez, N., Pey, J., Cusack, M., Reche, C., Querol, X., Alastuey, A., and Viana, M.: Variability of particle number, black carbon, and PM_{10}, $PM_{2.5}$, and PM_1 levels and speciation: influence of road traffic emissions on urban air quality, Aerosol Sci. Technol., 44, 487–499, doi:10.1080/02786821003758286, 2010.

Qin, Y. and Xie, S. D.: Spatial and temporal variation of anthropogenic black carbon emissions in China for the period 1980–2009, Atmos. Chem. Phys., 12, 4825–4841, doi:10.5194/acp-12-4825-2012, 2012.

Rajot, J. L., Alfaro, S. C., Gomes, L., and Gaudichet, A.: Soil crusting on sandy soils and its influence on wind erosion, Catena, 53, 1–16, 2003.

Reddy, M. S., Boucher, O., Bellouin, N., Schulz, M., Balkanski, Y., Dufresne, J. L., and Pham, M.: Estimates of global multicomponent aerosol optical depth and direct radiative perturbation in the Laboratoire de Meteorologie Dynamique general circulation model, J. Geophys. Res.-Atmos., 110, D10S16, doi:10.1029/2004jd004757, 2005.

Remer, L. A., Kaufman, Y. J., Tanre, D., Mattoo, S., Chu, D. A., Martins, J. V., Li, R. R., Ichoku, C., Levy, R. C., Kleidman, R. G., Eck, T. F., Vermote, E., and Holben, B. N.: The MODIS aerosol algorithm, products, and validation, J. Atmos. Sci., 62, 947–973, 2005.

Rodgers, C. D.: Inverse Methods for Atmospheric Sounding: Theory and Practice, World Sci., Tokyo, Japan, 240 pp., 2000.

Roney, J. A. and White, B. R.: Estimating fugitive dust emission rates using an environmental boundary layer wind tunnel, Atmos. Environ., 40, 7668–7685, doi:10.1016/j.atmosenv.2006.08.015, 2006.

Smith, S. J., van Aardenne, J., Klimont, Z., Andres, R. J., Volke, A., and Delgado Arias, S.: Anthropogenic sulfur dioxide emissions: 1850–2005, Atmos. Chem. Phys., 11, 1101–1116, doi:10.5194/acp-11-1101-2011, 2011.

Sow, M., Alfaro, S. C., Rajot, J. L., and Marticorena, B.: Size resolved dust emission fluxes measured in Niger during 3 dust storms of the AMMA experiment, Atmos. Chem. Phys., 9, 3881–3891, doi:10.5194/acp-9-3881-2009, 2009.

Streets, D. G., Yarber, K. F., Woo, J. H., and Carmichael, G. R.: Biomass burning in Asia: annual and seasonal estimates and atmospheric emissions, Global Biogeochem. Cy., 17, 1–20, doi:10.1029/2003gb002040, 2003.

Streets, D. G., Wu, Y., and Chin, M.: Two-decadal aerosol trends as a likely explanation of the global dimming/brightening transition, Geophys. Res. Lett., 33, 1–4, doi:10.1029/2006gl026471, 2006.

Streets, D. G., Yu, C., Wu, Y., Chin, M., Zhao, Z., Hayasaka, T., and Shi, G.: Aerosol trends over China, 1980–2000, Atmos. Res., 88, 174–182, 2008.

Streets, D. G., Yan, F., Chin, M., Diehl, T., Mahowald, N., Schultz, M., Wild, M., Wu, Y., and Yu, C.: Anthropogenic and natural contributions to regional trends in aerosol optical depth, 1980–2006, J. Geophys. Res.: Atmos., 114, 1–16, doi:10.1029/2008jd011624, 2009.

Sweeney, M., Etyemezian, V., Macpherson, T., Nickling, W., Gillies, J., Nikolich, G., and McDonald, E.: Comparison of PI-SWERL with dust emission measurements from a straight-line field wind tunnel, J. Geophys. Res.: Earth Surf., 113, 1–12, doi:10.1029/2007jf000830, 2008.

Szopa, S., Balkanski, Y., Schulz, M., Bekki, S., Cugnet, D., Fortems-Cheiney, A., Turquety, S., Cozic, A., Déandreis, C., Hauglustaine, D., Idelkadi, A., Lathière, J., Lefevre, F., Marchand, M., Vuolo, R., Yan, N., and Dufresne, J. L.: Aerosol and ozone changes as forcing for climate evolution between 1850 and 2100, Clim. Dynam., 1–28, doi:10.1007/s00382-012-1408-y, 2012.

Tegen, I., Harrison, S. P., Kohfeld, K., Prentice, I. C., Coe, M., and Heimann, M.: Impact of vegetation and preferential source areas on global dust aerosol: results from a model study, J. Geophys. Res.-Atmos., 107, 4576, doi:10.1029/2001jd000963, 2002.

Textor, C., Schulz, M., Guibert, S., Kinne, S., Balkanski, Y., Bauer, S., Berntsen, T., Berglen, T., Boucher, O., Chin, M., Dentener, F., Diehl, T., Easter, R., Feichter, H., Fillmore, D., Ghan, S., Ginoux, P., Gong, S., Grini, A., Hendricks, J., Horowitz, L., Huang, P., Isaksen, I., Iversen, I., Kloster, S., Koch, D., Kirkevåg, A., Kristjansson, J. E., Krol, M., Lauer, A., Lamarque, J. F., Liu, X., Montanaro, V., Myhre, G., Penner, J., Pitari, G., Reddy, S., Seland, Ø., Stier, P., Takemura, T., and Tie, X.: Analysis and quantification of the diversities of aerosol life cycles within AeroCom, Atmos. Chem. Phys., 6, 1777–1813, doi:10.5194/acp-6-1777-2006, 2006.

van Aardenne, J. A., Dentener, F. J., Olivier, J. G. J., Goldewijk, C. G. M. K., and Lelieveld, J.: A $1^\circ \times 1^\circ$ resolution data set of historical anthropogenic trace gas emissions for the period 1890–1990, Global Biogeochem. Cy., 15, 909–928, doi:10.1029/2000gb001265, 2001.

van der Werf, G. R., Randerson, J. T., Giglio, L., Collatz, G. J., Kasibhatla, P. S., and Arellano Jr, A. F.: Interannual variability in global biomass burning emissions from 1997 to 2004, Atmos. Chem. Phys., 6, 3423–3441, doi:10.5194/acp-6-3423-2006, 2006.

van der Werf, G. R., Randerson, J. T., Giglio, L., Collatz, G. J., Mu, M., Kasibhatla, P. S., Morton, D. C., DeFries, R. S., Jin, Y., and van Leeuwen, T. T.: Global fire emissions and the contribution of deforestation, savanna, forest, agricultural, and peat fires, Atmos. Chem. Phys., 10, 11707–11735, doi:10.5194/acp-10-11707-2010, 2010.

van Vuuren, D. P., Edmonds, J., Kainuma, M., Riahi, K., Thomson, A., Hibbard, K., Hurtt, G., Kram, T., Krey, V., Lamarque, J.-F., Masui, T., Meinshausen, M., Nakicenovic, N., Smith, S., and Rose, S.: The representative concentration pathways: an overview, Clim. Change, 109, 5–31, doi:10.1007/s10584-011-0148-z, 2011.

Vermote, E., Ellicott, E., Dubovik, O., Lapyonok, T., Chin, M., Giglio, L. and Roberts, G. J.: An approach to estimate global biomass burning emissions of organic and black carbon from MODIS fire radiative power, J. Geophys. Res., 114, D18205, doi:10.1029/2008jd011188, 2009.

Vernier, J. P., Thomason, L. W., Pommereau, J. P., Bourassa, A., Pelon, J., Garnier, A., Hauchecorne, A., Blanot, L., Trepte, C., Degenstein, D., and Vargas, F.: Major influence of tropical volcanic eruptions on the stratospheric aerosol layer during the last decade, Geophys. Res. Lett., 38(12), L12807, doi=10.1029/2011gl047563, 2011.

Wang, R., Tao, S., Shen, H., Wang, X., Li, B., Shen, G., Wang, B., Li, W., Liu, X., Huang, Y., Zhang, Y., Lu, Y., and Ouyang, H.: Global emission of black carbon from motor vehicles from 1960 to 2006, Environ. Sci. Technol., 46, 1278–1284, doi:10.1021/es2032218, 2011.

Yumimoto, K., Uno, I., Sugimoto, N., Shimizu, A., and Satake, S.: Adjoint inverse modeling of dust emission and transport over East Asia, Geophys. Res. Lett., 34, L08806, doi:10.1029/2006gl028551, 2007.

Yumimoto, K., Uno, I., Sugimoto, N., Shimizu, A., Liu, Z., and Winker, D. M.: Adjoint inversion modeling of Asian dust emission using lidar observations, Atmos. Chem. Phys., 8, 2869–2884, doi:10.5194/acp-8-2869-2008, 2008.

Zender, C. S., Miller, R. L. R. L., and Tegen, I.: Quantifying mineral dust mass budgets: terminology, constraints, and current estimates, Eos T. Am. Geophys. Union, 85, 509–512, doi:10.1029/2004eo480002, 2004.

Zhang, J. and Reid, J. S.: MODIS aerosol product analysis for data assimilation: assessment of over-ocean level 2 aerosol optical thickness retrievals, J. Geophys. Res.: Atmos., 111, 1–17, doi:10.1029/2005jd006898, 2006.

Zhang, J. L., Reid, J. S., Westphal, D. L., Baker, N. L., and Hyer, E. J.: A system for operational aerosol optical depth data assimilation over global oceans, J. Geophys. Res.-Atmos., 113, D10208, doi:10.1029/2007jd009065, 2008.

Zhang, Q., Streets, D. G., Carmichael, G. R., He, K. B., Huo, H., Kannari, A., Klimont, Z., Park, I. S., Reddy, S., Fu, J. S., Chen, D., Duan, L., Lei, Y., Wang, L. T., and Yao, Z. L.: Asian emissions in 2006 for the NASA INTEX-B mission, Atmos. Chem. Phys., 9, 5131–5153, doi:10.5194/acp-9-5131-2009, 2009.

Zhang, S., Penner, J. E., and Torres, O.: Inverse modeling of biomass burning emissions using Total Ozone Mapping Spectrometer aerosol index for 1997, J. Geophys. Res.-Atmos., 110, D21306, doi:10.1029/2004jd005738, 2005.

Zhu, S., Butler, T., Sander, R., Ma, J., and Lawrence, M. G.: Impact of dust on tropospheric chemistry over polluted regions: a case study of the Beijing megacity, Atmos. Chem. Phys., 10, 3855–3873, doi:10.5194/acp-10-3855-2010, 2010.